Title: Topical, immunomodulatory epoxy-tiglianes induce biofilm disruption and healing in acute and chronic skin wounds‡

Authors: Lydia C. Powell[1,2*†], Jason K. Cullen[3,4†], Glen M. Boyle[3,4], Tom De Ridder[5], Pei-Yi Yap[3], Wenya Xue[1], Carly J. Pierce[3], Manon F. Pritchard[1], Georgina E. Menzies[6], Muthanna Abdulkarim[7], Jennifer Y. M. Adams[1], Joana Stokniene[1], Lewis W. Francis[2], Mark Gumbleton[7], Jenny Johns[3], Katja E. Hill[1], Adam V. Jones[8], Peter G. Parsons[3], Paul Reddell[5], David W. Thomas[1].

Affiliations:

[1]Advanced Therapies Group, Cardiff University School of Dentistry; Cardiff, CF14 4XY, UK.

[2]Centre for Nanohealth, Swansea University Medical School, Swansea University; Swansea SA2 8PP, UK.

[3]Drug Discovery Group, QIMR Berghofer Medical Research Institute; Brisbane, Queensland 4006, Australia.

[4]School of Biomedical Sciences, Faculty of Medicine, University of Queensland; Brisbane, Queensland 4072, Australia.

[5]QBiotics Group Limited; Yungaburra, Queensland 4884, Australia.

[6]School of Biosciences, Cardiff University; Cardiff, CF10 3AX, UK.

[7]School of Pharmacy and Pharmaceutical Sciences, Cardiff University; Cardiff, CF10 3NB, UK.

[8]Oral Pathology, Cardiff and Vale University Health Board; Cardiff, CF14 4XY, UK.

*Corresponding author. Email: Powelllc1@cardiff.ac.uk

†These authors contributed equally to this work.

‡This manuscript has been accepted for publication in Science Translational Medicine. This

One Sentence Summary: Epoxy-tiglianes represent a non-antibiotic approach to treat acute and chronic wounds through targeted biofilm disruption and innate immune induction.

Abstract:

The management of antibiotic-resistant, bacterial biofilm infections in chronic skin wounds is an increasing clinical challenge. Despite advances in diagnosis, many patients do not derive benefit from current anti-infective/antibiotic therapies. Here we report a novel class of naturally occurring and semisynthetic epoxy-tiglianes, derived from the Queensland blushwood tree (*Fontainea picrosperma),* and demonstrate their antimicrobial activity (modifying bacterial growth and inducing biofilm disruption), with structure/activity relationships established against important human pathogens. In vitro, the lead candidate EBC-1013 stimulated protein kinase C (PKC)-dependent neutrophil reactive oxygen species (ROS) induction and NETosis, and increased expression of wound healing-associated cytokines, chemokines and antimicrobial peptides in keratinocytes and fibroblasts. In vivo, topical EBC-1013 induced rapid resolution of infection with increased matrix remodeling in acute thermal injuries in calves. In chronically infected, diabetic mouse wounds, treatment induced cytokine/chemokine production, inflammatory cell recruitment and complete healing (in six of seven wounds) with ordered keratinocyte differentiation. These results highlight a nonantibiotic approach involving contrasting, orthogonal mechanisms of action combining targeted biofilm disruption and innate immune induction in the treatment of chronic wounds.

Main Text:

INTRODUCTION

Chronic, nonhealing skin wounds are a major cause of morbidity/mortality, with estimated annual costs > $96.8 billion (*1*); diabetic foot ulcers (DFUs) alone affect >25% of diabetic patients (*2*) and 5-year mortality rates exceed those of prostate and breast cancer (*3*). Within these wounds, bacterial pathogens exist in organized biofilm communities, encased in a complex extracellular polymeric substance (EPS) matrix (*4*). Bacterial biofilm-associated infection represents an important clinical and therapeutic challenge, with bacteria demonstrating increased tolerance to antibiotic/antimicrobial therapy (*5*), entering dormant, persister states (*6*), and able to dysregulate local host-mediated immune responses (*7*). Wound biofilms also act as reservoirs of antimicrobial resistance (AMR) in hospital/community settings, fostering potential for spread via horizontal gene transfer (*8*). The importance of identifying alternative, nonantibiotic therapies to treat infection and limit AMR is increasingly recognized, e.g. phage therapy (*9*), quorum sensing inhibition (*10*) and probiotics (*11*). Novel strategies to reduce biofilm development and stimulate appropriate patient host responses would provide considerable therapeutic benefit.

Plants have evolved sophisticated mechanisms to resist pathogens including: targeted lysis, chemical inhibition, and modification of virulence factors and metabolism e.g. via RNA interference (*12, 13*). Phytochemicals, therefore, represent attractive therapeutic candidates for antibacterial applications. Although numerous candidates have been identified via high-throughput screening (*14, 15*), clinical translation has been complicated by toxicity, definition of structure/activity relationships (SARs), and pharmacoeconomic considerations (*16*).

Recently, a novel diterpene ester EBC-46 (tigilanol tiglate) from the Queensland blushwood tree (*Fontainea picrosperma*) has been the subject of considerable interest in the local treatment of solid tumors. EBC-46 has a multifactorial mode of action in tumor

destruction, associated with the activation of protein kinase C (PKC; *17, 18*) and potentially other C1 domain containing proteins. Unexpectedly, EBC-46 has also demonstrated utility in infected, nonhealing soft-tissue wounds in companion animals unresponsive to routine therapy, resulting in resolution of infection and induction of healing, with minimal scarring (*19*).

We hypothesized that these agents facilitate wound healing by induction of a successful immune response and modification of the wound biofilm. Using a panel of epoxy-tiglianes to identify SARs, we defined their antibiofilm activity and studied immunomodulation and healing induced by the lead candidate in acute (thermal) and chronic (diabetic) wounds. We describe here EBC-1013 for the treatment of chronic bacterial wound infection.

RESULTS

Epoxy-tiglianes interact with the bacterial cell membrane

To investigate whether the effects of EBC-46 in infected, nonhealing veterinary wounds (Fig. 1A) was mediated, in part, via a direct effect on wound bacteria, we explored the interaction of natural and semisynthetic epoxy-tiglianes (EBC compounds) against a range of common Gram-positive and Gram-negative wound pathogens. Three EBC structures with modifications in the C12/C13 ester linkages were used with identical total polar surface area (163.12 $A^{\circ 2}$; Fig. 1B and table S1). These included EBC-46, the prototype natural epoxy-tigliane (562.64 g/mol); EBC-1013, a semisynthetic epoxy-tigliane with C12 and C13 dihexanoate ester chains (592.72 g/mol); and EBC-147, a naturally occurring epoxy-tigliane with a C12 propanoate ester and C13 methylbutyrate ester (536.61 g/mol). The phorbol ester PMA (phorbol 12-myristate 13-acetate) was used as a PKC-activator control (*17, 18*).

Firstly, interaction of epoxy-tiglianes with the lipopolysaccharide-1,2-dipalmitoyl-3-phosphatidyl-ethanolamine (LPS-DPPE) bilayer membrane of the common wound pathogen *Pseudomonas aeruginosa* (mimicking the Gram-negative PAO1 bacterial outer membrane)

was characterized using molecular dynamics (MD) simulations. The simulations suggested that EBC-46 became embedded in the membrane bilayer (Fig. 1C), penetrating to a depth of 16 nm, whereas EBC-147 and EBC-1013 displayed more surface interactions, being unable to penetrate beneath the LPS molecular surface (fig. S1, A to C). Within the first 20 ns of the simulation, all three compounds became closely associated with/bound to the LPS-DPPE bilayer, remaining there for the duration (Fig. 1D). The time taken for this to occur differed for each compound, being the longest for EBC-1013. The mean distance measured between the agents and the LPS-DPPE bilayer indicated that EBC-1013 and EBC-147 remained closer to the bilayer during the simulation compared to EBC-46 (fig. S1D). Longer interaction times with the bacterial outer membrane (LPS-DPPE layer) were observed with 2-(2-L-alanyl)-2-deoxy-D-galactosamine (WLL; EBC-46) and 0-α-D-glucose (0GA; EBC-1013) surface residues (fig. S1E). EBC-147 overall showed the largest number of interacting residues, (fig. S1F), particularly with the surface residues 0-β-glucose (0GB), 2-α-L-rhamnose (2HA), 6-α-D-glucose (6GA) and phosphate (PO4), as well as nonsurface 6GB and WLL. The predicted and experimentally derived hydrophobic (lipophilic) properties of the epoxy-tiglianes revealed that all compounds had a log P > 0 (EBC-1013 > EBC-46 > EBC-147; table S1 and fig. S1G) indicative of hydrophobic compounds soluble in the lipid phase, with low solubility in the aqueous phase.

Having observed the resolution of infection and induction of healing within dermal wounds and predicted interaction of the epoxy-tiglianes with the Gram-negative bacterial cell membrane, we hypothesized that the mechanism of healing reflected direct antibacterial/antibiofilm activity (Fig 1E) and the induction of the innate immune system, with recruitment/activation of polymorphonuclear leukocytes (PMNLs) previously demonstrated in a solid tumor study (*17*).

Epoxy-tiglianes demonstrate antimicrobial activity against planktonic bacteria and biofilm formation

Susceptibility testing showed that the epoxy-tiglianes differed markedly in their ability to inhibit planktonic growth of Gram-positive bacteria [methicillin-resistant *Staphylococcus aureus* (MRSA) and *Streptococcus pyogenes*]. EBC-46 and EBC-1013 exhibited an MIC (minimum inhibitory concentration) range of 128 to 512 μg/ml, whereas EBC-147 demonstrated no MIC (>512 μg/ml; table S2). Notably, no MICs were obtained against Gram-negative strains (*P. aeruginosa*, *Escherichia coli* and *Acinetobacter baumannii*; MIC >512 μg/ml). Bacterial proliferation [adenosine triphosphate (ATP)] assays with *P. aeruginosa* and *E. coli* revealed no reduction in growth in the presence of the epoxy-tiglianes, demonstrating that epoxy-tigliane treatment did not inhibit or reduce Gram-negative bacterial growth/cell viability (fig. S2A) at both 4 hour (*E. coli*) and 6 hour (*P. aeruginosa*) time points (fig. S2B). Motility studies revealed that EBC-1013 altered the swarming motility pattern of *P. aeruginosa* to produce longer, thinner branching fingers, resulting in a significant reduction in surface area at 18 hours, compared to the untreated and vehicle (ethanol) controls ($P = 0.019$; Fig. 2, A and B and fig. S2C). Both EBC-1013 and EBC-46 treatment also resulted in a reduction in circularity at 18 hours, however, this effect was not significant (Fig. 2B). Extracellular virulence factor production assays in *P. aeruginosa* revealed that EBC-1013 significantly reduced pyocyanin production at both 24 and 48 hour time points, while EBC-1013 and EBC-46 treatment significantly reduced rhamnolipid production after 48 hours ($P \leq 0.017$; Fig. 2C). Cell membrane permeabilization studies demonstrated a significant increase in membrane permeability with EBC-46 and EBC-1013 treatment in *P. aeruginosa* (512 μg/ml), *S. aureus* (256 and 32 μg/ml respectively) and *E. coli* (EBC-1013 alone; 512 μg/ml) compared to the untreated and vehicle (ethanol) controls in planktonic culture ($P \leq 0.0021$; Fig. 3A). EBC-147

had no effect on cell membrane permeabilization in Gram-negative bacterial strains but permeabilized *S. aureus* cells at 512 μg/ml.

The effect of the epoxy-tiglianes on biofilm formation was studied using confocal laser scanning microscopy (CLSM) and COMSTAT image analysis (Fig. 3B). Whilst biofilm biovolume and thickness were similar in both untreated and epoxy-tigliane treated Gram-negative (fig. S3) and Gram-positive bacterial biofilms (fig. S4), strain-specific significant increases in the number of nonvital cells (DEAD:LIVE cell ratio) within *E. coli* and *S. aureus* biofilms were observed ($P < 0.0001$; Fig. 3C).

Epoxy-tiglianes induce biofilm disruption against established biofilm structures

The ability of the epoxy-tiglianes to disrupt established bacterial biofilms in a range of Gram-positive and Gram-negative bacteria was also studied using CLSM (Fig. 4A and fig. S5A). COMSTAT image analysis demonstrated significant strain-specific reductions in biofilm biovolume ($P \leq 0.023$; Fig. 4B) and thickness ($P \leq 0.042$; fig. S5B) after epoxy-tigliane treatment (256 μg/ml). EBC-46 demonstrated antibiofilm effects against Gram-negative biofilms alone (*A. baumannii* and *E. coli*) whilst EBC-147 treatment demonstrated more modest antibiofilm effects against Gram-negative *E. coli* and Gram-positive *S. pyogenes* biofilms. In contrast, EBC-1013 demonstrated antibiofilm effects in a wide range of Gram-positive (*S. pyogenes*) and Gram-negative biofilms (*A. baumannii*, *E. coli* and *P. aeruginosa*).

The effect of the epoxy-tiglianes on the biofilm EPS matrix was assessed using a multiple particle tracking (MPT) assay (Fig. 4C and fig. S5C). Epoxy-tigliane treatment significantly increased the diffusion coefficient of the nanoparticles within the *E. coli* biofilm ($P < 0.0001$; table S3), which was associated with alterations in the mechanical structure of the treated biofilm, with an up to 80-fold increase in creep compliance (Fig. 4D). EBC-1013 treatment was the most effective in increasing nanoparticle diffusion and creep compliance in *E. coli* biofilms, followed by EBC-46 and EBC-147.

To understand the effect of these agents on established biofilms, cell surface charge (zeta-potential) and hydrophobicity measurements were performed on *E. coli* cells. Here, no effect of epoxy-tigliane treatment on cell surface charge was evident (Fig. 4E), and EBC-46 alone induced changes in *E. coli* hydrophobicity where the cell surface became distinctly more hydrophilic when compared to the untreated and vehicle (ethanol) controls (Fig. 4F).

EBC-1013 induces activation of PMNLs and PBMCs in vitro

As other epoxy-tiglianes activate PKC (and potentially other C1 domain-containing proteins), the effect of EBC-1013, in which antibiofilm activity had been demonstrated (vide supra), on mammalian PMNLs and peripheral blood mononuclear cells (PBMCs) was studied. EBC-1013 was a potent respiratory burst inducer in PMNLs with an EC_{50} of 6.8 ng/ml, versus 1.1 ng/ml with PMA (Fig. 5A). EBC-1013-induced ROS (reactive oxygen species) production was PKC-dependent, as pre-treatment with the PKC-inhibitor BisI (Bisindolylmaleimide-I) prevented dihydroethidium (DHE) oxidation and fluorescence. EBC-1013 treatment induced ROS production in PMNLs over a wide range of concentrations (2.96 to 29,600 ng/ml; Fig. 5, B to D) and induced PMNL extracellular trap (NET) formation (at 3 to 6 hours; Fig. 5, C and D) in a dose-dependent manner. At the highest concentration (296,000 ng/ml), PMNL necrosis was evident, the observed loss of ROS production (Fig. 5B) reflected in diffuse Hoescht and SYTOX Green nuclear staining (Fig. 5D). At necrotic doses (≥ 74,000 ng/ml), EBC-1013 also significantly stimulated release of the antimicrobial peptide LL-37 from PMNLs ($P \leq 0.0052$; Fig. 5E). Furthermore, EBC-1013 significantly stimulated interleukin-1β (IL-1β) and IL-8 secretion from PBMCs at concentrations of ≥29.6 ng/ml ($P \leq 0.0290$; Fig. 5F).

EBC-1013 promotes resolution of infection in an acute burn wound model

The effect of EBC-1013 on the resolution of infection and wound healing was assessed in an immunocompetent bovine (calf disbudding) wound model (fig. S6, A to D). Following acute

thermal injury, animals were left untreated or were treated with a single, topical application of EBC-1013 (600 μg) or vehicle-only control. Clinical infection and wound surface area were then measured over 28 days (Fig. 6A and fig. S6E). On day 7, postoperative infection developed in all animals, characterized by purulent exudate from the wound eschar. Microbiological analysis revealed a microflora predominantly composed of *S. aureus* and heavy, mixed growth of anaerobes, including the bovine pathogen *Trueperella pyogenes*. At day 14, differences in wound area following treatment were evident between EBC-1013-treated wounds (71%) compared to vehicle-only (89%) and untreated (97%) groups (Fig. 6B). Differences in the persistence of clinical wound infection were also evident; purulent exudate and eschar were present in 100% of untreated animals, 83% of the vehicle-only control group and 33% of EBC-1013-treated animals (Fig. 6C). At day 28, rapid resolution of infection in EBC-1013-treated wounds was reflected in wound closure, with healing evident in 75% of wounds in the EBC-1013 group versus 25% of the untreated control wounds (fig. S6F). At 28 days, histological analysis demonstrated a marked increase in wound maturation, with reestablishment of more mature dermal collagen architecture in EBC-1013-treated wounds (Fig. 6, D and E). Reepithelialization/healing in the control animals was shown to be defective compared to EBC-1013 treated wounds, typified by detachment of the epithelia from the underlying dermis on sectioning (Fig. 6D) and a corresponding persistence of chronic inflammatory cells (lymphocytes, plasma cells and macrophages) in the untreated wounds observed at day 28 (Fig. 6E and fig. S6G).

EBC-1013 induces host defense peptide and cytokine/chemokine expression in primary keratinocytes and fibroblasts

To understand how EBC-1013 promotes wound healing in vivo, microarray analysis of primary human epidermal keratinocytes (HEKa) and dermal fibroblasts (HDFa) treated with EBC-1013 (100 ng/ml) was performed in vitro. Ingenuity Pathway Analysis (IPA) and Gene Ontology

(GO) enrichment analysis of EBC-1013-induced changes in HEKa (Fig. 7A) and HDFa (Fig. 7B) cells at 4 hours demonstrated the rapid induction of genes involved in leukocyte migration, the recruitment of phagocytes/leukocytes, angiogenesis/vasculogenesis and cytokine signaling pathways, respectively. Closer analysis of selected genes from the microarray dataset and quantitative polymerase chain reaction (qPCR) validation of several of these in HEKa cells (*B2M* normalization; Fig. 7C and fig. S7A) confirmed that EBC-1013 induced rapid (> 2 hours) expression of key host-defense peptide and cytokine/chemokine/growth factor genes involved in antimicrobial defense (*DEFB4*, *DEFB103A*, *DEFB104A* and *RNASE7*), leukocyte recruitment/proliferation/survival (*TNF*, *IL1B*, *IL17C*, *IL36B/G, CXCL8/IL8*, *IL24, CCL20* and *CSF2*), resolution of inflammation (*IL1RN, IL1F5* and *SLPI*) and angiogenesis (*VEGFB* and *VEGFC*). Normalization of qPCR target genes to *GAPDH* showed similar results (fig. S7B). Interestingly, there appeared to be temporal separation between induction of proinflammatory genes, which occurred at earlier time points (2 to 8 hours), versus host defense peptide and resolution genes (>8 hours), suggesting that the drug may induce an acute inflammatory response followed by a rapid resolution phase. LEGENDplex analysis confirmed changes in expression of IL-1β, IL-1RN, CXCL5 (CXC chemokine ligand 5), CXCL8/IL-8 and CCL20 (CC chemokine ligand 20) proteins, with similar temporal differences observed (Fig. 7C and fig. S7C). Similar changes were also observed in HDFa cells. These included up-regulation of *IL1B*, *IL6*, *IL24*, *CXCL8/IL-8, CXCL10, CXCL12, CCL20* and *VEGFA*, the majority observed by both microarray and qPCR analyses (Fig. 7D and fig. S7D to F). Again, normalization of qPCR target genes to *GAPDH* showed similar results (fig. S7E). All gene expression changes confirmed by qPCR in fibroblasts correlated with changes in cognate protein, apart from *IL1B* where up-regulation of protein was not observed and *CXCL1*, where protein secretion was induced in the absence of transcriptional up-regulation (Fig. 7D). EBC-

1013 exhibited limited effects on cellular viability over a longer exposure time of 72 hours (fig. S8).

IPA and GO enrichment analysis of changes induced at 48 hours indicated that EBC-1013 directed responses in HEKa and HDFa cells transitioned to the up-regulation of other key wound repair pathways, including formation of skin, skin/epidermis development, keratinocyte differentiation, extracellular matrix (ECM) organization and cell movement of granulocytes. Analysis of gene expression changes responsible for the skin development GO signature revealed large-scale up-regulation of late cornified envelope (*LCE*), cytokeratin (*KRT*) and small proline rich protein (*SPRR*) genes in HEKa cells. *LOR* and *FLG* were also stimulated in response to EBC-1013 treatment, suggesting a movement towards terminal differentiation (fig. S9A). In HDFa cells, EBC-1013 administration induced up-regulation of ECM organization-related genes including: *FN1*, *TNC, LAMC1* and *COL6A3* (fig. S9B).

EBC-1013 promotes resolution of infection and wound closure in chronic *db/db* wounds

The effect of EBC-1013 on chronic wounds in vivo was assessed in an established diabetic murine (*db/db*) model of chronic wounds, characterized by biofilm infection at the wound site (*20*). Wounds were treated with vehicle or EBC-1013 (50 µl of 0.3 mg/ml; days 1, 8 and 13). Wound area was recorded, and biopsies taken when macroscopic healing was evident in treated animals (fig. S10A). Application of EBC-1013 induced clinical wound closure in five of seven animals within 21 to 29 days of wounding (Fig. 8A) and wound reepithelialization (Fig. 8B and fig. S10B). In contrast, only one of seven in the vehicle-treated control group showed evidence of partial closure ($P < 0.01$).

EBC-1013 induces cytokine and chemokine gene expression in chronic *db/db* wounds

Analysis of EBC-1013-treated *db/db* wound biopsies (24 hours; fig. S11A) using qPCR partially-reflected the in vitro HEKa/HDFa data (Fig. 7) when normalized to *B2m* (Fig. 8, C to

E) or *Gapdh* (fig. S11, B to D). Employing a candidate approach, *Defb3* (the murine *DEFB4* ortholog: $P = 0.0333$), *Rnase6* (the *RNASE7* ortholog; $P = 0.0211$), *Camp* [the cathelicidin ortholog of human cationic antimicrobial protein of 18 kDa (CAP18); $P = 0.0128$], *Tnf* ($P = 0.0090$), *Il6* ($P = 0.0018$), *Il36g* ($P = 0.0152$), *Il1b* ($P = 0.0051$), *Il1rn* ($P = 0.0005$), *Cxcl2* ($P = 0.0011$) and *Ly6g* ($P < 0.0001$) were all significantly up-regulated in EBC-1013 treated wounds at 24 hours (Fig. 8, C to E). *Il33, Ccl20, Cxcl1* and *Cxcl10* were also up-regulated, although these changes were not significant at 24 hours (Fig. 8D). Some targets up-regulated by EBC-1013 treatment in HEKa/HDFa cells (*IL17C, IL24 and IL36B*) were not elevated in murine wounds at 24 hours (Fig. 8D), including *Adgre1* (F4/80) expression (indicative of macrophage recruitment) (Fig. 8E).

EBC 1013-induced *db/db* wound healing is associated with inflammatory cell recruitment and keratinocyte differentiation

Histology and immunohistochemistry of *db/db* wound biopsies revealed that EBC-1013 treatment was associated with induction of inflammation, with migration of $Ly6G^+$ cells (PMNLs and granulocytes) into the wound bed at 24 hours and suppuration, absent in vehicle-treated controls (Fig. 8F). Histological examination revealed complete reepithelialization in four of seven EBC-1013-treated wounds, which was absent in vehicle-treated wounds (Fig. 8G); >50% of EBC-1013 treated mice experienced complete wound closure with an absence of ulceration histologically. Marked differences in wound ulceration clinically (reflecting incomplete reepithelialization) between the vehicle control and EBC-1013-treated wounds were observed (2.60 ± 0.31 versus 0.92 ± 0.36 respectively; $P = 0.0011$; Fig. 8H). No differences, however, were observed in the numbers of chronic inflammatory cells (macrophages, lymphocytes and plasma cells) in the dermis at >21 days (Fig 8H). Histochemical staining also revealed that EBC-1013-treated cases were characterized by increased maturation of connective tissue and collagen production (Fig. 8H; 1.40 ± 0.27 versus

2.58 ± 0.42; $P = 0.0075$) with corresponding reduction in visible granulation tissue (3.00 ± 0.30 versus 2.08 ± 0.43; $P = 0.0286$) compared to vehicle treated controls.

DISCUSSION

Novel antimicrobial agents that target both the pathogen and host represent an exciting alternative treatment strategy for combating AMR infections in chronic wounds (*21*). Immune modulation avoids the selective fitness pressures from which AMR is likely to arise (*22*). Here, we first determined whether resolution of chronic wounds observed in epoxy-tigliane-treated veterinary cases was related to direct and/or indirect antibacterial activity in a series of preclinical screening studies. MD simulations suggested interaction of the epoxy-tiglianes (EBC-46 and EBC-1013) with the outer LPS layer of the Gram-negative *P. aeruginosa*, highlighting their potential ability to cause membrane disruption. In Gram-negative wound pathogens (in planktonic systems), however, this binding failed to induce significant direct antibacterial activity as deduced from effects on bacterial viability and metabolism (MIC and ATP assays). In keeping with this observation, whilst MIC values were recorded for Gram-positive species, these were typically >4-fold greater than those of conventional antibiotics e.g. *S. pyogenes* (≤8 versus 128 μg/ml; *23*). Bacterial cell membrane permeabilization with epoxy-tigliane treatment also varied considerably between Gram-positive/Gram-negative species e.g. *S. aureus* (≥ 32 μg/ml) and *E. coli*/*P. aeruginosa* (≥ 512 μg/ml). The marked differences in MIC between the bacterial species likely reflect increased permeability of the Gram-positive cell wall peptidoglycan layer (≤50,000 g/M), contrasting with the lipid rich outer membrane of Gram-negative bacteria (*24*). These results for the Gram-positive species (and those from the subsequent biofilm experiments for both Gram-positive and Gram-negative bacterial species) confirmed SARs between the side-chain length at the epoxy-tigliane C12 ester and biological activity (*18, 25*). EBC-147, with a short C12 ester chain, and low PKC activity, demonstrated

minimal anti-microbial activity. The semi-synthetic EBC-1013, however, with long side chains at C12 and C13 [C12 C13 dihexanoate] exhibited increased anti-microbial and anti-biofilm activity when compared to EBC-46 (despite demonstrating similar PKC activation).

Failing to demonstrate a significant, direct antimicrobial effect on Gram-negative bacteria, we hypothesized the antimicrobial effect observed in vivo reflected disruption of the bacterial biofilm within the wound-bed. In chronic wounds, bacteria are embedded in a complex, charged, EPS matrix, composed of both host- and bacterial-derived extracellular DNA (*4*), which plays an important structural role in resisting therapy, both as a physiochemical barrier to diffusion (of immune cells and antimicrobial agents) but also in dysregulating the local immune response (*26, 27*). In chronic wound models, bacterial biofilms formed from *P. aeruginosa* and *S. aureus* have even demonstrated enhanced tolerance to PMNL-derived antibacterial activity (*28, 29*).

Biofilm formation assays showed that whilst there was little inhibition of biofilm growth with epoxy-tigliane treatment, clear, strain-specific decreases in cell viability were evident. As disruption of established infections was evident in the animal wounds, we examined the ability of the agents to disrupt established bacterial biofilms. Here, the ability of epoxy-tiglianes to disrupt established biofilms was demonstrated, with striking, (strain-specific) reductions in bacterial biofilm volume in both Gram-positive and Gram-negative bacterial biofilms (with the exception of *S. aureus*). The extent of the biophysical disruption observed in CLSM imaging was reflected in MPT (*30*), with increased nanoparticle diffusion following epoxy-tigliane treatment, where EBC-1013 demonstrated the greatest increase in diffusion. These measurements are indicative of increased pore size within the treated biofilms due to disruption of the entangled EPS matrix. This result, combined with the lack of discernible effects of epoxy-tigliane treatment on *E. coli* cell surface charge and EBC-46 alone inducing increased cell-surface hydrophilicity, suggests that the anti-biofilm activity observed

in vitro was principally related to interactions with the mature (48 hours) EPS matrix. Targeted disruption of the biofilm EPS matrix may facilitate increased PMNL diffusion into biofilm structures, enhance PMNL mediated biomass reduction and increase antibiotic effectiveness (*31, 32*). Interestingly, the activity of the epoxy-tiglianes in the biofilm disruption and MPT experiments (EBC-1013>EBC-46>EBC-147) reflects their predicted and experimentally derived hydrophobicity (log *P*) (*18*). A similar association between side chain hydrophobicity and antibacterial activity has been described in antimicrobial peptides (*33, 34*).

Whilst the antibiofilm effects of the epoxy-tiglianes may be important in mediating chronic wound healing, previous studies have highlighted the ability of the EBC-46 to promote wound healing after intratumoural injection in an oncology setting (*35*). EBC-46 has recently been registered by the U.S. Food and Drug Administration and the European Medicines Agency as a veterinary pharmaceutical (Stelfonta) (*19*) and is currently in human clinical trials. As a result, we sought to investigate the ability of the lead candidate identified in the microbiology experiments, EBC-1013, to modify mammalian cell responses involved in wound healing via functional changes in cell phenotype and gene/protein expression (*36, 37*). EBC-1013 treatment was found to promote ROS induction, NET formation and LL-37 (host defense peptide) release from PMNLs. ROS, in addition to displaying direct antimicrobial activity, may also act as a secondary messenger, regulating leukocyte recruitment and angiogenesis (*38*). Interestingly, whilst NETosis may impair the growth of *P. aeruginosa*, *S. aureus* and *E. coli* (*39*), pathogenic hyperstimulation of NETosis has been implicated in biofilm survival (*29, 40*) and inhibition of wound closure in DFUs (*41, 42*). Release of LL-37 (produced from cleavage of human cathelicidin CAP18) may also directly modulate immune cell function (*43, 44*), limit NET degradation by bacterial nucleases (*45*) and potentially inhibit biofilm formation (*46*). Topical LL-37 is currently undergoing assessment in patients with DFUs (www.clinicaltrials.gov, identifier: NCT04098562). The ability of EBC-1013 to

stimulate proinflammatory cytokine production (IL-1β and IL-8) from PBMCs was also evident.

The ability of EBC-1013 to induce dermal healing was then characterized in a calf-disbudding model. Marked clinical differences in wound healing were evident following single applications of EBC-1013 to 'nondressed' open wounds, typified by more rapid resolution of wound infection (day 14) and increased wound closure. Reorganization of collagen architecture within treated wound beds was accompanied by resolution of chronic inflammation at day 28. Maturation of the granulation tissue observed after treatment may reflect proinflammatory chemokine induction; effectively mediating fibroblast recruitment into the provisional wound matrix and transforming growth factor-β1 (TGF-β1) mediated matrix synthesis (*47*).

The effects of EBC-1013 on dermal fibroblasts and keratinocytes demonstrated early induction of proinflammatory cytokines/chemokines/growth factor genes, followed by up-regulation of host defense peptide, proresolution, keratinocyte differentiation and ECM organization genes. These data complement the in vivo calf disbudding studies, with induction of an initial acute inflammatory response, resolution of infection, followed by increased ECM production and keratinocyte differentiation (wound maturation). A recent single cell RNA sequencing study demonstrated that fibroblast subsets associated with healing in DFUs up-regulate or are predicted to up-regulate *FN1*, *IL6*, *CXCL12* and *VEGFA* (*48*), which were all induced by EBC-1013. Changes in *IL1β*, *CXCL1* and *CXCL2* expression have also been correlated with healing in venous leg ulcers (VLUs), suggesting that EBC-1013 may also provide clinical benefit to patients with this chronic wound type (*49*).

Whilst encouraging, calf disbudding wounds eventually heal within 6 weeks, irrespective of treatment, and fail to reproduce the protracted healing characteristic of human DFUs or VLUs (*50*). Hence, we additionally employed a chronic nonhealing biofilm wound

model based on the obese *db/db* mouse, where bacterial biofilm development occurs spontaneously following inhibition of antioxidant enzymes (*20*). Here, the effects of EBC-1013 application were marked with increased wound closure, ordered differentiation of the epithelium and restoration of the epithelial barrier evident macroscopically (and microscopically) in EBC-1013-treated mice. Consistent with the in vitro microarray data, qPCR analysis of EBC-1013-treated wounds demonstrated significant up-regulation of host defense peptides (*Defb3, Rnase6* and *Camp*) and proinflammatory cytokine/chemokines *(Tnf, Il1b, Il6*, *Il36g, Cxcl2*), in addition to *Il1rn* at 24 hours post treatment, with activation of a local innate immune response characterized by recruitment of PMNLs and granulocytes. The granulocyte chemoattractants (*Cxcl1* and *Cxcl2*) substitute for loss of the *IL8* gene ortholog in mice (*51, 52*). Activation of tumor necrosis factor (TNF) and IL-6 signaling, together with macrophage expression of IL-1β, are also associated with the healing of DFUs *(48*). There was also up-regulation of *Cxcl1* and *Ccl20* in the wound bed, where these genes are also associated with wound healing (*53*).

The marked effects on reepithelialization and differentiation reflect EBC-1013-induced up-regulation of *LCE*, *KRT* and *SPRR* genes in keratinocytes in vitro. EBC-1013 induction of *LOR* and *FLG* (encoding the epidermal structural proteins loricrin and profilligrin), suggested promotion of epithelial maturation/differentiation. Interestingly, several genes shown to be preferentially up-regulated in oral mucosal keratinocytes (*PITX*, *ALDH3A1*, *KRT13, KRT78, SPRR2A, SPRR2E, SPRR3, LCE3D* and *ATP1B1*) were also stimulated by EBC-1013 (*54*). EBC-1013 treatment effects on cellular migration may reflect the role of PKC in regulating cell surface dynamics and expression of syndecan, β1 integrin and CD44 (*55*). Thomason et al. (*56*) highlighted the role of PKCα modulation in wound healing, with active PKCα in transgenic mice inducing wound reepithelialization. Interestingly, EBC-46-induced, PKC-

dependent keratinocyte migration in monolayer scratch wounds has also recently been described (*57*).

Although healing with induction of acute inflammation appears counter intuitive due to the role of oxidative stress in the development of chronic wounds (*58*), healing of DFUs and VLUs following compression therapy has been shown to occur with the onset of acute inflammation (*59*). Moreover, previous studies have demonstrated down-regulation of *CXCL1* in fibroblasts within the chronic wound bed (*36*). Sawaya et al. (*60*) showed reduced PMNL and macrophage recruitment in DFUs compared to acute oral and skin wounds; RNA sequencing analysis demonstrated that *TNFα*, *CSF2*, *IL6*, *DEFB4* and a general inflammatory response were suppressed in DFUs compared to acute skin wounds. Within *db/db* wounds, induction of PMNL chemokines *Cxcl1* and *Cxcl2,* with corresponding induction of proinflammatory and host defense peptide gene expression in vivo, effectively overcomes locally dysregulated immune cell recruitment/responses in the wound bed. Here, the biofilm related disruption of the wound microbiome by EBC-1013, with the acute oxidative burst, keratinocyte and fibroblast gene induction, may initiate bacterial clearance, wound reepithelialization and wound remodeling. Clinically, this may be important as chronic wound recurrence in humans is characterized by bacterial/biofilm persistence and impaired keratinocyte differentiation/barrier function (*61*).

The in vivo results here were particularly encouraging as the EBC-1013 was applied topically, without surgical intervention in the calf model and without debridement in the diabetic mouse model. All experiments employed distinct vehicle-only controls to ensure that the observed effects were unrelated to the ethanol (in vitro) or the gel (consisting of propylene glycol, hydroxypropyl methylcellulose and sodium citrate) employed in the in vivo calf and diabetic mouse wound models. The direct translation of these results from animal models of wound healing to human chronic wounds however, is challenging in an aged population. In

these patients, in addition to bacterial infection, extensive injury and diabetes (modeled here), additional confounding factors exist. These include not only age-related (matrix and biochemical) changes in the dermis, but also contemporaneous polypharmacy and coexisting macrovascular pathology, e.g. ischaemia.

Importantly, the toxicity profile of topically administered epoxy-tigliane structures is favorable. Panizza et al (*35*) in a phase 1 intradermal injection study of the tigilanol tiglate (EBC-46) failed to establish a maximum tolerated dose. The strong epidermal localization of topically applied PMA (with structural similarity to EBC-1013) has also been demonstrated by Li et al (*62*).

EBC-1013 is proposed as a safe, topical treatment candidate with multimodal functions; disrupting bacterial biofilms and directing an acute inflammatory response to initiate wound healing, combining resolution of inflammation, promotion of ECM production and keratinocyte differentiation. This candidate is now in clinical development.

MATERIALS AND METHODS

Study design

Following the resolution of an epoxy-tigliane-treated chronic soft tissue wound in an observational canine study, the primary goal of this study was to identify the antimicrobial, antibiofilm and immunomodulatory activity of the epoxy-tiglianes (EBC-46, EBC-1013 and EBC-147) in vitro and identify a lead candidate to study in vivo. The interaction of the epoxy-tigliane structures with the bacterial membrane was defined using MD modeling, and their antimicrobial activity was evaluated in MIC, growth and virulence factor production assays. Antibiofilm activity was assessed by cell motility and both biofilm formation and disruption assays (using CLSM image analysis and MPT) against a range of wound pathogens. Immune induction of the lead candidate EBC-1013 was studied in PMNL and PBMC populations in

vitro (ROS production, LL-37 release, NET generation and cytokine/chemokine release) and in human keratinocytes and fibroblasts using expression profiling, qPCR and cytokine/chemokine bead arrays.

The effect of the lead candidate EBC 1013 versus vehicle-only and untreated controls was studied in acute thermal injury in a calf disbudding model (analyzed clinically and histologically in n = 12 wounds per treatment; alpha .05; power 90%). The ability of topical EBC-1013 to induce dermal healing in chronic, nonhealing infected *db/db* mouse wounds was studied versus vehicle-only controls (n = 7 animals; alpha .05; power 90%). Wound healing, remodeling and reepithelialization were analyzed clinically and histologically in these nonblinded and nonrandomized studies. Host defense peptide and cytokine/chemokine expression, together with immune cell recruitment were analyzed by qPCR and immunohistochemistry (n = 10 to 14 wounds per treatment; alpha .05; power 90%). These studies were intended to provide the preclinical data to justify human clinical trials.

Animal experiments were performed in strict accordance with the recommendations of the Australian Code for the Care and Use of Animals for Scientific Purposes of the National Health and Medical Research Council of Australia (*63)*. All bovine protocols were reviewed and approved by the Queensland Government Department of Agriculture and Fisheries Animal Ethics Committee (SA 2018/11/667; CA 2017/10/1119). All murine protocols were reviewed and approved by the QIMR Berghofer Medical Research Institute Animal Ethics Committee, approval number A0106-042M.

Epoxy-tiglianes

The prototypical epoxy-tigliane EBC-46 (also known as tigilanol tiglate) was compared to the naturally occurring EBC-147 and the semisynthetic EBC-1013. The phorbol di-ester PMA (Sigma-Aldrich), a known PKC activator, was used as a control in the ROS production assay (*17,18*). The compounds were solubilized in 100% ethanol and vehicle (ethanol) equivalent

controls were used throughout. The epoxy-tiglianes were supplied by QBiotics Group Ltd. The physicochemical properties of the epoxy-tigliane compounds were calculated using the SwissADME computational chemistry website (*64*).

MD simulation

MD simulations were performed with epoxy-tigliane molecules and a Gram-negative LPS (LPS-DPPE) lipid layer, to mimic the *P. aeruginosa* PAO1 outer membrane. Standard MD protocols were followed using AMBER based force field parameters and thermally equilibrated coordinates reported for the LPS-DPPE membrane (*65*). Simulations were performed using the GROMACS MD software (*66*). Extra solute was added using the GROMACS module to cover the epoxy-tiglianes along with the LPS-DPPE membrane. The particle mesh Ewald method was used to treat long-range electrostatic interactions and a 1.4 nm cutoff was applied to Lennard-Jones interactions. Simulations were performed in the NPT (isothermal-isobaric) ensemble, under periodic boundary conditions, at a temperature of 310 K, and a pressure of 1 atm. Each simulation was performed using a three-step process: the steepest descent energy minimization with a tolerance of 1000 KJ^{-1} nm^{-1}; a pre MD run with 25,000 steps at 0.002 /s per step making a total of 2500 ps; an MD stage run for a total of 300 ns. Root mean square deviation was monitored along with the total energy, pressure and volume of the simulation to monitor the stability of the simulations. Molecular graphic images were generated using the Molecular Operating Environment (*67*). Contact maps were produced using the CONAN contact analysis tools (*68*). A cutoff of 5 Å was used and a truncation life time of 0.5 was selected, this ensured that only physically meaningful interaction types (classified as hydrophobic, hydrogen bond and salt bridge) with contact probabilities of more than 50% were taken into account.

Bacterial strains

The following human wound pathogens were used: *P. aeruginosa* PAO1, *E. coli* IR57 (V7; *69*), MRSA 1004A (*70*), *S. pyogenes* E80 (chronic leg wound isolate; this study) and *A. baumannii* 7789 (V19; *69*). Bacterial colonies were grown on blood agar no. 2 (BA; Lab M) supplemented with 5% horse blood. Overnight cultures were grown in tryptone soya broth (TSB; Lab M) at 37°C, with shaking. Cultures were adjusted to 10^7 colony-forming units (CFU)/ml (optical density at wavelength 600 nm of 0.05) before use in the following experiments.

Antimicrobial susceptibility testing

Conventional broth microdilution MIC assays (*71*) of the epoxy-tiglianes were performed in line with standard guidelines (*72*) in cation-adjusted Mueller-Hinton (MH) broth (Lab M) against the human wound pathogens, alongside vehicle (ethanol) equivalent controls (n=3).

Pyocyanin and rhamnolipid production assay

Overnight cultures of *P. aeruginosa* PAO1 were adjusted to 6×10^{11} CFU/ml, and 30 µl was added to MH broth (3 ml) allowing for 24 hours growth with 256 µg/ml epoxy-tiglianes (EBC-46, EBC-1013, EBC-147) or vehicle (ethanol) equivalent treatment. Bacterial cultures were centrifuged (10,000 *g*) for 10 min to produce a cell-free culture supernatant. For the pyocyanin assay, chloroform (3:2, v/v) was used for the extraction of pyocyanin pigment. Pyocyanin (in the chloroform-phase) was then reextracted with 0.2 M HCl (2:1, v/v) and the absorbance was read at 520 nm. For the rhamnolipid assay, diethyl ether (1:1, v/v) was used for the extraction and the extract was dried before reconstitution in deionized water (200 µl). Then, 50 µl of the reconstituted extract was added to 450 µl of 0.19% orcinol (w/v) in H_2SO_4 (1:1, v/v) before heating at 80°C for 30 min. After cooling to room temperature, the absorbance was read at 421 nm (n=3).

Microbial cell viability assay

Growth curves measuring ATP production were performed using the BacTiter-Glo microbial cell viability assay (Promega), to assess the antimicrobial activity of the three compounds (EBC-46, EBC-147 and EBC-1013) at 0, 2, 4, 6, 8, 12, 24, 48 and 72 hours, with luminescence (relative light units) read on a FLUOstar Omega plate reader (n=3).

Membrane permeability assay

Cell permeability following epoxy-tigliane treatment (16 to 512 µg/ml) was determined using SYTOX Green Nucleic Acid Stain (Thermo Fisher Scientific) as previously described (*73*). A positive control [70% (v/v) isopropanol; IPA], untreated control and vehicle (ethanol) equivalent controls were also included (n=3).

Biofilm formation and disruption assays

Biofilm formation was assessed over 24 hours in 96-well glass-bottom plates in MH broth as previously described (*74*) ± EBC-46, EBC-1013 or EBC-147 [256 µg/ml or at the MIC value (*S. aureus* only)] or vehicle (ethanol) equivalents at 37ºC. Biofilm disruption was assessed in established (24 hours) biofilms where 50% of the supernatant was replaced with fresh MH broth as previously described (*74*) ± EBC-46, EBC-1013 and EBC-147 (256 µg/ml) or a vehicle equivalent (ethanol) and incubated a further 24 hours at 37ºC. Biofilms were stained with LIVE/DEAD BacLight stain and phosphate-buffered saline (PBS) was added to each well before imaging with z-stack CLSM (n=3). The resultant images were analyzed by COMSTAT software (*75*) to produce measurements of biofilm biomass and DEAD/LIVE ratio as previously described (*74*).

Analysis of cytokine release from PBMCs

PBMCs were isolated from human heparinized blood (acquired from n=3 donors; two male and one female) by Ficoll-Paque sedimentation (*76*). Briefly, whole blood was diluted 3:1 in

prewarmed Roswell Park Memorial Institute (RPMI)-1640 medium and layered on top of Ficoll-Paque. Samples were centrifuged at 400 *g*, after which the PBMC layer was extracted, washed three times with RPMI-1640 and resuspended in RPMI-1640 supplemented with 10% (v/v) fetal calf serum (FCS). PBMCs were seeded at a density of 1.5×10^5 cells per well in media and stimulated with compound at 296, 29.6 and 2.96 ng/ml in duplicate for 24 hours. Media samples were taken from each of the required wells and frozen at -80°C until use. Each media sample was assayed for the presence of IL-1β and IL-8 using the BD Cytometric Bead Array (CBA) Human Inflammatory Cytokine Detection Kit and an LSR Fortessa flow cytometer according to the manufacturers' instructions (Becton Dickinson). Mean fluorescence intensity values from each sample were compared against a standard curve to determine cytokine concentrations in cell culture supernatants (pg/ml ± SD; standard deviation) using Flow Cytometric Analysis Program (FCAP) Array v3.0 software.

PMNL isolation

PMNLs were isolated from human peripheral venous blood (n=4 donors; two male and two females) using density-dependent centrifugation. Briefly, PBMCs were first removed from whole blood (50 ml) as detailed above. The red blood cell/granulocyte pellet from this step was resuspended in 12.5 ml of 4% dextran and 0.85% NaCl by end-over-end mixing. Following gravity-based sedimentation at room temperature to separate most erythrocytes from granulocytes (for approximately 20 min), the supernatant was removed, and a crude neutrophil pellet was obtained via centrifugation (1000 rpm, 5 min, 20°C). The remaining erythrocytes were lysed by resuspending the pellet in 13 ml of 0.2 × PBS and gently inverting the tube for 100 s. Isotonicity was reestablished through the addition of 4.4 ml of 3% NaCl, 10 ml of 1 × PBS and 1 mM EDTA, after which a pellet of pure granulocytes/neutrophils was acquired, again through centrifugation at 1000 rpm, 5 min, at 20°C. Cells were subsequently washed once in Hanks buffered saline (HBSS) without Ca^{2+} or Mg^{2+}, centrifuged as above, and then

resuspended in either HBSS (with Ca^{2+}/Mg^{2+}), 2% FCS or RPMI-1640, 10% FCS (inactivated at 70°C) dependent on the experiment.

NETosis/necrosis assays

PMNLs (from n=3 human donors; two males and one female) were resuspended at 1.1×10^6 cells/ml in RPMI-1640, 10% FCS (heat inactivated at 70°C) containing a 1:50,000 dilution of Hoechst (10 mg/ml of stock) and SYTOX Green (5 mM stock). The cell suspension (10^5 cells; 90 µl) was seeded into the individual wells of a black, clear bottom 96-well plate (Corning #3603) and incubated at 37°C, 5% CO_2 for 5 min. Serial dilutions of EBC-1013 were compiled (10 × final assay concentration) in RPMI medium (vide supra) and 10 µl was added to the required wells in duplicate. Vehicle-only (ethanol) controls were also included. Plates were subsequently incubated at 37°C, 5% CO_2 and Hoechst/SYTOX Green fluorescence images were recorded for each well at 1, 3 and 6 hours using an INCell Analyzer 2000 (GE Healthcare) with a 10x objective. Individual Hoechst and SYTOX Green images were combined using ImageJ, after which the percentage of NETs (Hoechst positive and SYTOX Green positive cells) in each composite image were was quantified using a custom script developed in QuPath image analysis software (*77*).

LL-37 release assays

PMNLs (n=4 human donors: two males and two females) were resuspended in RPMI-1640, 10% FCS (heat inactivated at 70°C) and 10^5 cells were seeded into the wells of a clear 96-well plate (90 µl; Corning #3595). Serial dilutions of EBC-1013 (10× final concentration), with vehicle (ethanol) controls, were prepared as previously described and 10 µl was aliquoted into the required wells in duplicate. Plates were incubated for 3 hours (37°C, 5% CO_2) after which supernatants (90 µl) were removed from each well and centrifuged in a V-bottom plate to remove cell debris. The cell-free supernatant was then removed from each well and LL-37 release was quantified using an enzyme-linked immunosorbent assay (ELISA) kit (Hycult

Biotech). Absorbance readings were normalized to vehicle-only controls to determine fold increases in LL-37 release.

Cell culture

Adult HEKa (Thermo Fisher Scientific, #C0215C) and HDFa (Thermo Fisher Scientific, #C0135C) were cultured in EpiLife Basal Medium supplemented with S7 and gentamicin/amphotericin B and Medium 106 supplemented with low serum growth supplement (LSGS), gentamycin, respectively (Thermo Fisher Scientific). T25 flasks (Nunc) were coated with a Coating Matrix kit (Thermo Fisher Scientific) for 0.5 hours at room temperature prior to HEKa culture. Cells were maintained in a humidified incubator (37°C, 5% CO_2) and passaged using tryspin/versene at 80% confluency. All cell lines were confirmed mycoplasma negative prior to use using MycoAlert (Promega). Both HEKa and HDFa were used between passage 3 (p 3) and p10 for all assays.

Microarray assays

HEKa and HDFa were seeded into T25 flasks (Nunc) at a density of 2.5×10^4 cells per flask (5 ml). After reaching 80% confluency, the growth medium was aspirated and replaced with 5 ml of fresh medium containing vehicle (ethanol) or 100 ng/ml EBC-1013. At 0, 0.5, 1, 2, 4, 8, 24, 48 and 72 hours, the growth medium was aspirated, cells were washed twice with fresh medium and the total RNA was extracted from each sample using a QIAGEN RNeasy mini kit as per the manufacturer's instructions. Briefly, 350 µl of buffer RLT containing β-mercaptoethanol was added to each flask and cells were scraped into a 1.5 ml microfuge tube (Eppendorf). Following a freeze/thaw cycle, RNA was extracted and purified according to the kit protocol. RNA concentration was subsequently determined using a NanoDrop 2000 (Thermo Fisher Scientific), after which biotinylated complementary RNA (cRNA) was prepared using the Illumina TotalPrep RNA Amplification Kit (Ambion). Labeled cRNA was hybridized to HumanHT-12 v4 BeadChip Arrays containing 47,323 elements representing all

known genes (Illumina). Expression data was extracted in GenomeStudio (Illumina) using default analysis settings and the no normalization method. Resulting data were imported into GeneSpring GX (Agilent Technologies) for quantile normalization with default settings. Significantly different gene expression values were initially selected using a moderated t-test at $P < 0.05$ for treatment pairs (vehicle versus treated). A 2-fold cut-off filter for any one of the treatment pairs was then applied to identify significantly different gene expression. Log_2 FC values were calculated from these data for heatmap generation using GraphPad Prism v8.0.

qPCR analysis of HEKa/HDFa cells

HEKa and HDFa were plated into T25 flasks and treated with vehicle (ethanol) or 100 ng/ml EBC-1013 as detailed above. At 0, 8, 24 and 48 hours, medium was removed from each flask, flash-frozen in dry ice and stored at -80°C in preparation for cytokine/chemokine analysis using a BioLegend LEGENDplex bead array kit. The remaining cells were washed twice with fresh medium and RNA extracted (vide supra). Then, 500 ng of RNA was utilized for cDNA synthesis using SuperScript III Reverse Transcriptase (Life Technologies) according to manufacturer's instructions. Resultant cDNA samples were diluted 1:25 into a SYBR Green PCR Master Mix (Applied Biosystems) and run in triplicate using 384-well plates in a CFX384 Touch Real-Time PCR Detection system. Primers directed against the housekeeping genes *GAPDH* and *B2M* were used for normalization. The ΔΔCt was used for data analysis. Cq values from each timepoint were taken and normalized to the mean Cq (quantification cycle) values from *GAPDH* and *B2M* data and $2^{-\Delta\Delta Ct}$ values were calculated using the mean of normalized triplicate Cq values. The primers used in all cell-based qPCR studies are detailed in table S4. Log_2 FC values were calculated from these data for heatmap generation using GraphPad Prism v8.0.

Analysis of cytokine/chemokine expression in HEKa/HDFa culture supernatants

Media isolated during culture of HEKa/HDFa with EBC-1013 (see 'qPCR analysis of HEKa/HDFa cells') was thawed prior to analysis using a custom-designed LEGENDplex bead analysis kit (Biolegend). The following cytokines/chemokines were analysed using a LSR Fortessa flow cytometer according to the manufacturer's instructions: IL-1β, IL-6, IL-8, IL-33, IL-1RA, CXCL1, CXCL5, CXCL10, CCL20, VEGFA. Log_2 FC values were calculated from these data for heatmap generation using GraphPad Prism v8.0.

Acute wound model

An acute burn wound healing model was studied (in a non-randomized, non-blinded study) following the routine practice of thermal disbudding of female Holstein Friesian dairy calves at 2-3 months of age. Following sedation by intramuscular injection using 0.6 ml of 20 mg/ml xylazine hydrochloride (Ilium Xylazil-20, Troy Laboratories Pty Ltd) and a cornual nerve block using 4 ml of 20 mg/ml lignocaine hydrochloride (Ilium Lignocaine 20, Troy Laboratories Pty Ltd), pre-disbudding biopsies were taken before horn buds were bilaterally ablated with a 240 V electric disbudding iron (at ≥500°C) applied to each site for <10 s (mean 8 ±3 s). The burn wounds were treated with 200 µl vehicle-only controls (80% w/w propylene glycol, 1.5% w/w hydroxypropyl methylcellulose, 20% v/v 10 mM sodium citrate pH 3.11); 600 µg EBC-1013 in 200 µl vehicle or untreated. Swabs were taken of the bovine wounds and both aerobic and anaerobic bacterial culture performed by IDEXX (New South Wales, Australia). Digital imaging was employed to study inflammation, re-epithelialization and wound contraction, on days 7, 14 and 28 post-injury. Subsequent biopsies were performed under local anaesthesia, using 4 ml of 20 mg/ml lignocaine hydrochloride injected as a cornual nerve block on days 7, 14 and once healed at day 28**.**

Chronic diabetic wound model

All mice were housed and bred in a specific pathogen-free (SPF) facility, with 12-hour light/12-hour dark cycle and continual access to food and water, until initiation of the chronic wound

protocol. In efficacy-based experiments, diabetic B6.BKS(D)-*Lepr*^{db}/J homozygote mice (referred to as *db/db*; mice >6 months in age, males and females) were transferred from an SPF facility and housed for 6-8 weeks in nonsterile conditions (nonsterile environment, bedding, food and water) prior to wounding (*20*). Mice were treated intraperitoneally with a catalase inhibitor (1 g/kg of aminotriazole; Sigma-Aldrich) 20 min prior to wounding, after which a 6 mm diameter full-thickness, punch-biopsy wound was made on the back of (isofluorane) anaesthetized animals. Immediately following this, all wounds were treated with a glutathione peroxidase (GPx) inhibitor (150 mg/kg of mercaptosuccinic acid; Sigma-Aldrich) that was administered topically around the edge of the wound site prior to dressing with Tegaderm (3 M). At 24 hours (day 1), the dressing was removed and mice were treated with approximately 50 µl vehicle [80% (w/w) propylene glycol, 1.5% (w/w) hydroxypropyl methylcellulose, 20% (v/v) 10 mM sodium citrate (pH 3.11)] or EBC-1013 (300 µg/ml in identical vehicle) and redressed with Tegaderm. Wounds were subsequently re-treated on days 8 and 13. Wounds were measured directly after removal of Tegaderm and photographed. An excisional biopsy was acquired at the end of the experiment between days 21 and 29.

For molecular analysis of wound samples after EBC-1013 administration, separate *db/db* mice were treated as above and tissue biopsies were acquired after 24 hours. Biopsies were bisected through the wound site, both sides were flash-frozen [after embedding in optimal cutting temperature (OCT) compound] and stored at -80°C until use. In other experiments, the wound was fixed in 10% neutral-buffered formalin solution and processed for immunohistochemistry.

qPCR analysis of wound sections. For tissue-based analyses, 10 × 20 µm tissue sections were cut from fresh frozen wound samples (OCT embedded) treated with vehicle or EBC-1013 and RNA was extracted as detailed above. cDNA was generated from each sample using

SuperScript III Reverse Transcriptase (Life Technologies) and qPCR was performed as previously detailed above using the primers detailed in table S5.

Statistical analysis

When applicable, statistical analyses were undertaken using either using GraphPad Prism v8 or v9 software. Values represent either means ±SD (standard deviation) or means ±SEM (standard error of mean). For each test, $P < 0.05$ was considered significant. Normality assessment of the data (Shapiro-Wilk analysis) was performed to assess whether parametric or non-parametric statistical testing was appropriate. Statistical comparisons were assessed with either one-way or two-way analysis of variance (ANOVA) for multiple groups, using either Tukey's, Dunnett's or Sidak's multiple comparison tests. Non-parametric data was statistical compared using the Kruskal-Wallis test for multiple groups and Mann-Whitney U multiple comparison test. Specific tests are noted in each figure legend. Individual subject-level data for experiments where $n < 20$ are shown in data file S1.

Supplementary Materials

Materials and Methods

Figs. S1 to S11

Tables S1 to S5

MDAR Reproducibility Checklist

Data file S1

References

1. C. K. Sen, Human wounds and its burden: An updated compendium of estimates. *Adv. Wound Care* **8**, 39-48 (2019).

2. D. Martins-Mendes, M. Monteiro-Soares, E. J. Boyko, M. Ribeiro, P. Barata, J. Lima, R. Soares, The independent contribution of diabetic foot ulcer on lower extremity amputation and mortality risk. *J. Diabetes Complications* **28**, 632–638 (2014).

3. J. M. Robbins, G. Strauss, D. Aron, J. Long, J. Kuba, Y. Kaplan, Mortality rates and diabetic foot ulcers: Is it time to communicate mortality risk to patients with diabetic foot ulceration? *J. Am. Podiatr. Med. Assoc.* **98**, 489-493 (2008).

4. S. L. Percival, K. E. Hill, D. W. Williams, S. J. Hooper, D. W. Thomas, J. W. Costerton, A review of the scientific evidence for biofilms in wounds. *Wound Repair Regen* **20**, 647–657 (2012).

5. T-F. Mah, Biofilm-specific antibiotic resistance. *Future Microbiol.* **7**, 1061-1072 (2012).

6. S. L. Percival, K. E. Hill, S. Malic, D. W. Thomas, D. W. Williams, Antimicrobial tolerance and the significance of persister cells in recalcitrant chronic wound biofilms. *Wound Repair Regen.* **19**, 1-9 (2011).

7. J. F. Gonzalez, M. M. Hahn, J. S. Gunn, Chronic biofilm-based infections: skewing of the immune response. *Pathog. Dis*. **76**, fty023 (2018).

8. A. H. A. M. van Hoek, D. Mevius, B. Guerra, P. Mullany, A. P. Roberts, H. J. M. Aarts, Acquired antibiotic resistance genes: an overview. *Front. Microbiol.* **2**, 203 (2011).

9. F. L. Gordillo Altamirano, J. J. Barr, Phage therapy in the postantibiotic era. *Clin. Microbiol. Rev.* **32**, e00066-18 (2019).

10. B. Rémy, S. Mion, L. Plener, M. Elias, E. Chabrière, D. Daudé, Interference in Bacterial Quorum Sensing: A Biopharmaceutical Perspective. *Front. Pharmacol.* **9**, 203 (2018).

11. P. Markowiak, K. Slizewska, Effects of Probiotics, Prebiotics, and Synbiotics on Human Health. *Nutrients* **9**, 1021 (2017).

12. T. Muhammad, F. Zhang, Y. Zhang, Y. Liang, RNA Interference: A natural immune system of plants to counteract biotic stressors. *Cells* **8**, 38 (2019).

13. J. Huang, M. Yang, L. Lu, X. Zhang, Diverse Functions of Small RNAs in Different Plant–Pathogen Communications. *Front. Microbiol.* **7**, 1552 (2016).

14. M. Zampieri, B. Szappanos, M. V. Buchieri, A. Trauner, I. Piazza, P. Picotti, S. Gagneux, S. Borrell, B. Gicquel, J. Lelievre, B. Papp, U. Sauer, High-throughput metabolomic analysis predicts mode of action of uncharacterized antimicrobial compounds. *Sci. Transl. Med.* **10**, eaal3973 (2018).

15. J. W. Phillips, M. A. Goetz, S. K. Smith, D. L. Zink, J. Polishook, R. Onishi, S. Salow, J. Wiltsie, J. Allocco, J. Sigmund, K. Dorso, S. Lee, S. Skwish, M. de la Cruz, J. Martin, F. Vicente, O. Geniolloud, J. Lu, R. E. Painter, K. Young, K. Overbye, R. G. K. Donald, S. B. Singh, Discovery of kibdelomycin, a potent new class of bacterial type II topoisomerase inhibitor by chemical-genetic profiling in *Staphylococcus aureus*. *Chem. Biol.* **18**, 955–965 (2011).

16. F. Cappiello, M. R. Loffredo, C. Del Plato, S. Cammarone, B. Casciaro, D. Quaglio, M. L. Mangoni, B. Botta, F. Ghirga, The Revaluation of Plant-Derived Terpenes to Fight Antibiotic-Resistant Infections. *Antibiotics* **9**, 325 (2020).

17. G. M. Boyle, M. M. A. D'Souza, C. J. Pierce, R. A. Adams, A. S. Cantor, J. P. Johns, L. Maslovskaya, V. A. Gordon, P. W. Reddell, P. G. Parsons, Intra-Lesional Injection of the Novel PKC Activator EBC-46 rapidly ablates tumors in mouse models. *PLOS One* **9**, e108887 (2014).

18. J. K. Cullen, G. M. Boyle, P-Y. Yap, S. Elmlinger, J. L. Simmons, N. Broit, J. Johns, B. Ferguson, L. A. Maslovskaya, A. I. Savchenko, P. M. Mirzayans, A. Porzelle, P.

V. Berhardt, V. A. Gordon, P. W. Reddell, A. Pagani, G. Appendino, P. G. Parsons, C. M. Williams, Activation of PKC supports the anticancer activity of tigilanol tiglate and related epoxytiglianes. *Sci Rep* **11,** 207 (2021).

19. T. R. De Ridder, J. E. Campbell, C. Burke-Schwarz, D. Clegg, E. L. Elliot, S. Geller, W. Kozak, S. T. Pittenger, J. B. Pruitt, J. Riehl, J. White, M. L. Wiest, C. M. Johannes, J. Morton, P. D. Jones, P. F. Schmidt, V. Gordon, P. Reddell. Randomized controlled clinical study evaluating the efficacy and safety of intratumoral treatment of canine mast cell tumors with tigilanol tiglate (EBC-46). *J. Vet. Intern. Med.* 35, 415-429 (2021).
20. S. Dhall, D. C. Do, M. Garcia, J. Kim, S. H. Mirebrahim, J. Lyubovitsky, S. Lonardi, E. A. Nothnagel, N. Schiller, M. Martins-Green, Generating and Reversing Chronic Wounds in Diabetic Mice by Manipulating Wound Redox Parameters. *J. Diabetes Res.* 562625 (2014).
21. L. Czaplewski, R. Bax, M. Clokie, M. Dawson, H. Fairhead, V. A. Fischetti, S. Foster, B. F. Gilmore, R. E. W. Hancock, D. Harper, I.R. Henderson, K. Hilpert, B. V. Jones, A. Kadioglu, D. Knowles, S. Ólafsdóttir, D. Payne, S. Projan, S. Shaunak, J. Silverman, C. M. Thomas, T. J. Trust, P. Warn, J. H. Rex, Alternatives to antibiotics-a pipeline portfolio review. *Lancet Infect. Dis.* **16**, 239-251 (2016).
22. R. E. W. Hancock, A. Nijnik, D. J. Philpott, Modulating immunity as a therapy for bacterial infections. *Nat. Rev. Microbiology* **10**, 243 (2012).
23. The European Committee on Antimicrobial Susceptibility Testing. Breakpoint tables for interpretation of MICs and zone diameters. Version 11.0, 2021. http://www.eucast.org.
24. P. A. Lambert, Cellular impermeability and uptake of biocides and antibiotics in Gram-positive bacteria and mycobacteria. *J. Appl. Microbiol.* **92**, 46S-45S (2002).

25. A. Jonet, A. Dassonville-Klimpt, P. Sonnet, C. Mullié, Side chain length is more important than stereochemistry in the antibacterial activity of enantiomerically pure 4-aminoalcohol quinoline derviatives. *J. Antibiot.* **66**, 683-686 (2013).

26. C. Moser, H. T. Pedersen, C. J. Lerche, M. Kolpen, L. Line, K. Thomsen, N. Høiby, P. Ø. Jensen, Biofilms and host response – helpful or harmful. *APMIS* **125**, 320-338 (2017).

27. E. A. Grice, J. A. Segre, Interaction of the microbiome with the innate immune response in chronic wounds. *Adv. Exp. Med. Biol*. **946**, 55-68 (2012).

28. M. J. Pestrak, S. B. Chaney, H. C. Eggleston, S. Dellos-Nolan, S. Dixit, S. S. Mathew-Steiner, S. Roy, M. R. Parsek, C. K. Sen, D. J. Wozniak. *Pseudomonas aeruginosa* rugose small-colony variants evade host clearance, are hyper-inflammatory, and persist in multiple host environments. *PLOS Pathog*. **14**, e1006842 (2018).

29. M. Bhattacharya, E. T. M. Berends, R. Chan, E. Schwab, S. Roy, C. K. Sen, V. J. Torres, D. J. Wozniak, *Staphylococcus aureus* biofilms release leukocidins to elicit extracellular trap formation and evade neutrophil-mediated killing. *Proc. Natl. Acad. Sci. USA* **115**, 7416-7421 (2018).

30. L. C. Powell, M. Abdulkarim, J. Stokniene, Q. E. Yang, T. R. Walsh, K. E. Hill, M. Gumbleton, D. W. Thomas, Quantifying the effects of antibiotic treatment on the extracellular polymer network of antimicrobial resistant and sensitive biofilms using multiple particle tracking. *NPJ Biofilms Microbiomes* **7**, 13 (2021).

31. V. A. Ray, P. J. Hill, K. C. Stover, S. Roy, C. K. Sen, L. Yu, D. J. Wozniak, A. diGiandomenico, Anti-Psl Targeting of *Pseudomonas aeruginosa* biofilms for Neutrophil-Mediated disruption. *Sci. Rep*. **7**, 16065 (2017).

32. J. Geddes-McAlister, A. Kugadas, M. Gadjeva, Tasked with a challenging objective: Why do neutrophils fail to battle *Pseudomonas aeruginosa* biofilms. *Pathogens* **8**, 283 (2019).

33. J. R. Henriksen, T. Etzerodt, T. Gjetting, T. L. Andresen, Side chain hydrophobicity modulates therapeutic activity and membrane selectivity of antimicrobial peptide Mastoparan-X. *PLOS One* **9**, e1007 (2014).

34. Y. Chen, M. T. Guarieri, A. I. Vasil, M. L. Vasil, C. T. Mant, R. S. Hodges, Role of peptide hydrophobicity in the mechanism of action of α-helical antimicrobial peptides. *Antimicrob. Agents Chemother.* **51**, 1398-1406 (2007).

35. B. J. Panizza, P. de Souza, A. Cooper, A. Roohullah, C. S. Karapetis, J. D. Lickliter, Phase I dose-escalation study to determine the safety, tolerability, preliminary efficacy and pharmacokinetics of an intratumoral injection of tigilanol tiglate (EBC- 46). *EBioMedicine* **50**, 433–441 (2019).

36. I. B. Wall, R. Moseley, D. M. Baird, D. Kipling, P. Giles, I. Laffafian, P. E. Price, D. W. Thomas, P. Stephens, Fibroblast dysfunction is a key factor in the non-healing of chronic venous leg ulcers. *J Invest. Dermatol.* **128**, 2526-2540 (2008).

37. A. Ridiandries, J. T. M. Tan, C. A. Bursill, The role of chemokines in wound healing. *Int. J. Mol. Sci.* **19**, 3217 (2018).

38. C. Dunnill, T. Patton, J. Brennan, J. Barrett, M. Dryden, J. Cooke, D. Leaper, N. T. Georgopoulos, Reactive oxygen species (ROS) and wound healing: the functional role of ROS and emerging ROS-modulating technologies for augmentation of the healing process. *Int. Wound. J.* **14**, 89-96 (2017).

39. V. Delgado-Rizo, M. A. Martínez-Guzmán, L Iniguez-Gutierrez, A. García-Orozco, A. Alvarado-Navarro, M. Fafutis-Morris, Neutrophil extracellular traps and its implications in inflammation: An overview, *Front. Immunol.* **8**, 81 (2017).

40. J. Hirschfeld, Dynamic interactions of neutrophils and biofilms. *J Oral Microbiol.* 6 (2014).

41. S. L. Wong, M. Demers, K. Martinod, M. Gallant, Y. Wang, A. B. Goldfine, C. R. Kahn, D. D. Wagner, Diabetes primes neutrophils to undergo NETosis, which impairs wound healing. *Nat. Med.* **21,** 815–819 (2015).

42. G. P. Fadini, L. Menegazzo, M. Rigato, V. Scattolini, N. Poncina, A. Bruttocao, S. Ciciliot, F. Mammano, C. D. Ciubotaru, E. Brocco, M. C. Marescotti, R. Cappellari, G. Arrigoni, R. Millioni, S. V. de Kreutzenberg, M. Albiero, A. Avogaro, NETosis delays diabetic wound healing in mice and humans. *Diabetes* **65**, 1061-1071 (2016).

43. M. R. Scheenstra, R. M. van Harten, E. J. A. Veldhuizen, H. P. Haagsman, M. Coorens, Cathelicidins modulate TLR-activation and inflammation. *Front. Immunol.* **11**, 1137 (2020).

44. M. H. Braff, M. Zaiou, J. Fierer, V. Nizet, R. L. Gallo, Keratinocyte production of cathelicidin provides direct activity against bacterial skin pathogens. *Infect. Immun.* **73**, 6771-6781 (2005).

45. A. Neumann, L. Völlger, E. T. M. Berends, E. M. Molhoek, D. A. C. Stapels, M. Midon, A. Friães, A. Pingoud, S. H. M. Rooijakkers, R. L. Gallo, M. Mörgelin, V. Nizet, H. Y. Naim, M. von Köckritz-Blickwede, Novel role of the antimicrobial peptide LL-37 in the protection of neutrophil extracellular traps against degradation by bacterial nuleases. *J. Innate Immun.* **6**, 860-868 (2014).

46. J. Overhage, Human host defence peptide LL-37 prevents bacterial biofilm formation. *Infect. Immun.* **76**: 4176-4182 (2008).

47. P. Martin, R. Nunan, Cellular and molecular mechanisms of repair in acute and chronic wound healing. *Br. J. Dermatol.* **173**, 370-8 (2015).

48. G. Theocharidis, B. E. Thomas, D. Sarkar, H. L. Mumme, W. J. R. Pilcher, B. Dwivedi, T. Sandoval-Schaefer, R. F. Sîrbulescu, A. Kafanas, I. Mezghani, P. Wang, A. Lobao, I. S. Vlachos, B. Dash, H. C. Hsia, V. Horsley, S. S. Bhasin, A. Veves, M. Bhasin, Single cell transcriptomic landscape of diabetic foot ulcers. *Nat. Commun.* **13**, 181 (2022).

49. R. C. Stone, O. Stojadinovic, A. M. Rosa, H. A. Ramirez, E. Badiavas, M. Blumenberg, M. Tomic-Canic, A bioengineered living cell construct activates an acute wound healing response in venous leg ulcers. *Sci. Transl. Med.*, **9**, eaaf8611 (2017).

50. J. D. Raffetto, D. Ligi, R. Maniscalco, R. A. Khalil, F Mannello, Why Venous Leg Ulcers Have Difficulty Healing: Overview on Pathophysiology, Clinical Consequences, and Treatment. *J. Clin. Med.* **10**, 29 (2021).

51. W. S. Modi, T. Yoshimura, Isolation of novel GRO genes and a phylogenetic analysis of the CXC chemokine subfamily in mammals. *Mol. Biol. Evol.* **16**, 180-193 (1999).

52. K. Watanabe, M. Iida, K. Takaishi, T. Suzuki, Y. Hamada, Y. Iizuka, S. Tsurufuji, Chemoattractants for neutrophils in lipopolysaccharide-induced inflammatory exudate from rats are not interleukin-8 counterparts but gro-gene-product/melanoma-growth-stimulating-activity-related factors. *Eur. J. Biochem.* **214**, 267-270 (1993).

53. S. V. Prasad, K. Fiedoruk, T. Daniluk, E. Piktel, R. Bucki, Expression and Function of Host Defence Peptides at Inflammation Sites. *Int. J. Mol. Sci.* **21**, 104 (2020).

54. R. Iglesias-Bartolome, A. Uchiyama, A. A. Molinolo, L. Abusleme, S. R. Brooks, J. L. Callejas-Valera, D. Edwards, C. Doci, M-L Asselin-Labat, M. W. Onaitis, N. Moutsopoulos, J. S. Gutkind, M. I. Morasso, Transcriptional signature primes human oral mucosa for rapid wound healing. *Sci. Transl. Med.* **10**, eaap8798 (2018).

55. S. Kleiser, A. Nyström, Interplay between cell-surface receptors and extracellular matrix in skin. *Biomolecules* **10**, 1170 (2020).

56. H. A. Thomason, N. H. Cooper, D. M. Ansell, M. Chiu, A. J. Merrit, M. J. Hardman, D. R. Garrod, Direct evidence that PKCα positively regulates wound re-epithelialization: correlation with changes in desomosomal adhesiveness. *J. Pathol.* **227**, 346-356 (2012).

57. R. L. Moses, G. M. Boyle, R. A. Howard-Jones, R. J. Errington, J. P. Johns, V. Gordon, P. Reddell, R. Steadman, R. Moseley, Novel epoxy-tiglianes stimulate skin keratinocyte wound healing responses and re-epithelialization via protein kinase C activation. *Biochem. Pharmacol.* **178**, 114048 (2020).

58. J. H. Kim, B. Yang, A. Tedesco, E. G. D. Lebig, P. M. Ruegger, K. Xu, J. Borneman, M. Martins-Green, High levels of oxidative stress and skin microbiome are critical for initiation and development of chronic wounds in diabetic mice. *Sci. Rep.* **17**, 19318 (2019).

59. S. E. Herrick, P. Sloan, M. McGurk, L. Freak, C.N. McCollum, M. W. Ferguson, Sequential changes in histologic pattern and extracellular matrix deposition during the healing of chronic venous ulcers. *Am. J. Pathol.* **141**, 1085-1095 (1992).

60. A. P. Sawaya, R. C. Stone, S. R. Brooks, I. Pastar, I. Jozic, K. Hasneen, K. O'Neill, S. Mehdizadeh, C. R. Head, N. Strbo, M. I. Morasso, M. Tomic-Canic, Deregulated immune cell recruitment orchestrated by FOXM1 impairs human diabetic wound healing. *Nat Commun* **11,** 4678 (2020).

61. S. Roy, H. Elgharably, M. Sinha, K. Ganesh, S. Chaney, E. Mann, C. Miller, S. Khanna, V. K. Bergdall, H. M. Powell, C. H. Cook, G. M. Gordillo, D. J. Wozniak, C. K. Sen, Mixed-species biofilm compromises wound healing by disrupting epidermal barrier function. *J. Pathol.* **223**, 331 (2014).

62. L. Li, S. Shukla, A. Lee, S. H. Garfield, D. J. Maloney, S. V. Ambudkar, S. H. Yuspa. The skin cancer chemotherapeutic agent ingenol-3-angelate (PEP005) is a substrate for the epidermal multidrug transporter (ABCB1) and targets tumor vasculature. *Cancer Res.* **70**, 4509–4519 (2010).

63. National Health and Medical Research Council. Australian code for the care and use of animals for scientific purposes, 8th edition. (National Health and Medical Research Council, Canberra, 2013).

64. A. Daina, O. Michielin, V. Zoete, SwissADME: a free web tool to evaluate pharmacokinetics, drug-likeness and medicinal chemistry friendliness of small molecules. *Sci. Rep.* **7,** 42717 (2017).

65. K. N. Kirschner, R. D. Lins, A. Maass, T. A. Soares, A glycam-based force field for simulations of lipopolysaccharide membranes: Parametrization and validation. *J. Chem. Theory Comput.* **8**, 4719-4731 (2012).

66. M. J. Abraham, T. Murtola, R. Schulz, S. Páll, J. C. Smith, B. Hess, E. Lindahl, GROMACS: High performance molecular simulations through multi-level parallelism from laptops to supercomputer. *SoftwareX* **1-2,** 19-25 (2015).

67. *Molecular Operating Environment (MOE)*, 2019.01; Chemical Computing Group ULC, 1010 Sherbooke St. West, Suite #910, Montreal, QC, Canada, H3A 2R7, (2020).

68. D. Mercadante, F. Gräter, C. Daday, CONAN: A tool to decode dynamical information from molecular interaction maps. *Biophys. J.* **114**, 1267-1273 2018).

69. S. Khan, A. Tøndervik, H. Sletta, G. Klinkenberg, C. Emanuel, E. Onsøyen, R. Myrvold, R. A. Howe, T. R. Walsh, K. E. Hill, D. W. Thomas, Overcoming drug resistance with alginate oligosaccharides able to potentiate the action of selected antibiotics. *Antimicrob. Agents Chemother.* **56,** 5134–5141 (2012).

70. Howell-Jones, R. S., "Antibiotic use in the treatment of chronic wounds", thesis, Cardiff University, Cardiff, Wales, UK (2007); https://orca.cf.ac.uk/55708/1/U584227.pdf

71. J. H. Jorgensen, J. D. Turnidge, J. A. Washington, Antibacterial susceptibility tests: dilution and disk diffusion methods. in *Manual of Clinical Microbiology*, P. R. Murray, E. J. Baron, M. A. Pfaller, J. H. Jorgensen, R. H. Yolken, Eds (ASM Press, Washington, DC, ed. 7, 1999). [Seventh edition], pp. 1526–1543

72. Clinical and Laboratory Standards Institute, Methods for determining bactericidal activity of antimicrobial agents; approved guideline, (*CLSI document M26-A*. CLSI, Wayne, Pennsylvania, USA, 1999). https://clsi.org/media/2428/m26ae_sample.pdf

73. D. T. F. McLean, F. T. Lundy, D. J. Timson, IQ-motif peptides as novel anti-microbial agents. *Biochimie* **95**, 875-880 (2013).

74. L. C. Powell, M. F. Pritchard, E. Ferguson, K. Powell, S. U. Patel, P. D. Rye, S-M. Sakellakou, N. J. Buurma, C. D. Brilliant, J. M. Copping, G. E. Menzies, P. D. Lewis, K. E. Hill, D. W. Thomas, Targeted disruption of the extracellular polymeric network of *Pseudomonas aeruginosa* biofilms by alginate oligosaccharides. *NPJ Biofilms Microbiomes* **4**, 13 (2018).

75. A. Heydorn, A. Toftgaard Nielsen, M. Hentzer, C. Sternberg, M. Givskov, B. Kjær Ersbøll, S. Molin, Quantification of biofilm structures by the novel computer program COMSTAT. *Microbiology-SGM* **146**, 2395–2407 (2000).

76. S. K. Panda, B. Ravindran, Isolation of human PBMCs. *Bio-protocol* **3**, e323 (2013).

77. P. Bankhead, M. B. Loughrey, J. A. Fernández, Y. Dombrowski, D. G. McArt, P. D. Dunne, S. McQuaid, R. T. Gray, L. J. Murray, H. G. Coleman, J. A. James, M. Salto-

Tellez, P. W. Hamilton. QuPath: Open source software for digital pathology image analysis. *Sci. Rep.* **7**, 16878 (2017).

78. A. K. Marr, J. Overhage, M. Bains, R. E. W. Hancock, The Lon protease of *Pseudomonas aeruginosa* is induced by aminoglycosides and is involved in biofilm formation and motility. *Microbiology* **153**, 474-482 (2007).
79. R. L. Soon, J. Li, J. D. Boyce, M. Harper, B. Adler, I. Larson, R. L. Nation, Cell surface hydrophobicity of colistin-susceptible vs resistant *Acientobacter baumannii* determined by contact angles: methodological considerations and implications. *J. Appl. Microbiology* **113**, 940-951 (2012).
80. S. K. Suvarna, C. Layton, J. D. Bancroft. Bancroft's Theory and Practice of Histological techniques. 7th Edition. Nottingham. Churchill Livingstone. (2012).

Acknowledgements: We thank QBiotics Group Ltd for funding and Justine Campbell for clinical support with the calf model. The *db/db* diabetic mice are originally from the Jackson Laboratory #000697 and were obtained from Professor Peter Thorn, University of Queensland. We also thank the QIMR Berghofer Animal Facility for their help with diabetic mouse studies, together with QIMR Berghofer Histological Services and the QIMR Berghofer Flow Cytometry and Imaging Facility. IDEXX, Coorparoo DC, Queensland, performed the microbiological analysis of the calf wound samples. Computational resources and support was provided by the Supercomputing Wales project, which is part-funded by the European Regional Development Fund via the Welsh Government. We thank Tam H. Nguyen for the development of the NETosis script used in the QuPath analysis.

Funding:

Australian National Health and Medical Research Council Development Grant 1093569 (GMB, JKC, PGP, PR).

QBiotics Group Ltd, Queensland, Australia (LCP, JKC, GMB, MFP, KEH, PGP, PR, DWT).

ACCELERATE East programme, European Regional Development Fund Grant 515454 (DWT, LCP).

SMARTExpertise 2014-2020 West Wales and the Valleys, European Regional Development Fund Grant 2017/COL/004 (LWF).

Author contributions:

Funding acquisition: DWT, KEH, LCP, MFP, GMB, PGP, JKC, PR, LWF

Conceived and designed experiments: DWT, KEH, LCP, JKC, MG, GMB, PGP, TDR, MFP, GEM, PR

Performed the experiments: LCP, JKC, WX, P-YY, CJP, TDR, GEM, MA, JS, AVJ, JJ

Analysed the data: LCP, JKC, GMB, KEH, DWT, WX, P-YY, CJP, GEM, MA, JYMA, JS, AVJ, JJ

Contributed reagents/materials/analysis tools: PR, LWF

Wrote and edited the paper: LCP, DWT, KEH, JKC, GMB, WX, TDR, GEM, MA, JS, AVJ, PR

Competing interests: DWT, KEH, LCP, MFP, GMB, JKC and PGP received research funding from QBiotics. PR, TDR and PGP are paid employees of QBiotics Group Ltd, while PR, TDR, GMB, JKC, JJ, P-YY and PGP are shareholders in QBiotics Group Ltd. PR, PGP, DWT, KEH, LCP, MFP, GMB and JKC are inventors on the patent (2019902144 -Australia and PCT/AU2020/050623 -International) submitted by QBiotics Group that covers biofilm disruption. The other authors have no conflicts of interest to disclose.

Data and material availability: All data associated with this study are present in the paper or in the Supplementary Materials. MD simulation data is available on Zenodo (https:doi.org/10.5281/zenodo.6616259) and the expression profiling data is all contained under the GEO accession number superseries GSE202953. The QuPath script used for NETosis analysis is freely available at https://forum.image.sc/t/qupath-script-for-identification-of-netosis-in-isolated-pmnl-assays/70130?u=jason_cullen. Reagents will be made available by the corresponding author and request for epoxy-tigliane structures should be directed to the QBiotics Group.

Figures

Fig. 1

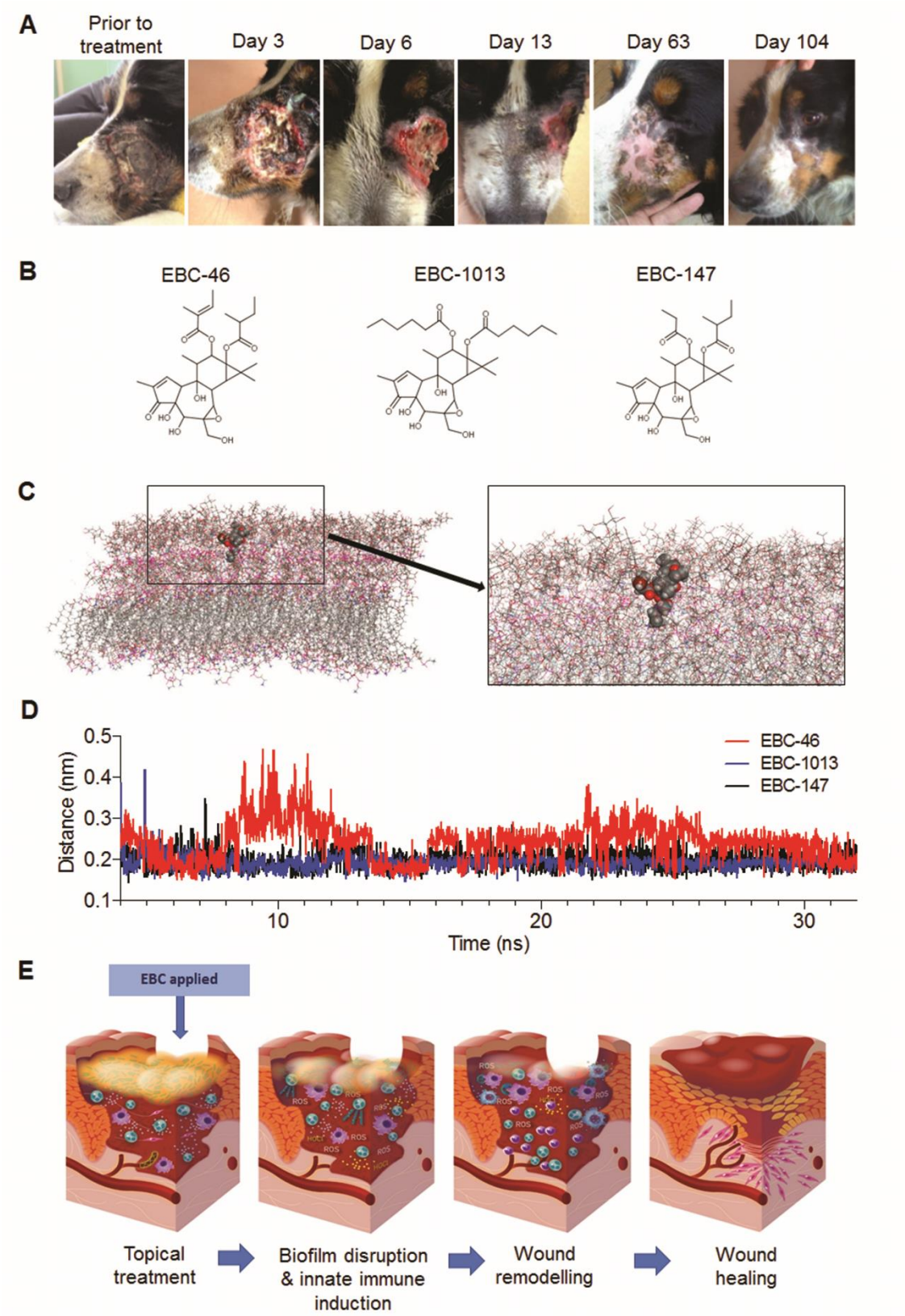

Fig. 1. Epoxy-tiglianes induce resolution of chronic infection and interact with the cell-surface of Gram-negative bacteria. (**A**) Photographs of the resolution of a chronic (3 month) necrosing ulcer, unresponsive to standard antibiotic and anti-inflammatory therapy, following treatment with the epoxy-tigliane EBC-46 in a canine veterinary case. (**B**) Chemical structure of three epoxy-tigliane candidate compounds (EBC-46, EBC-1013 and EBC-147). (**C**) Molecular dynamics (MD) simulations showing a molecular representation of EBC-46 buried within the *P. aeruginosa* PAO1 cell outer membrane (LPS-DPPE) bilayer (shown at a higher magnification in the inset). (**D**) Distance between epoxy-tiglianes (center mass) and the LPS-DPPE bilayer over time. The first 20 ns is shown for clarity, beyond which the EBCs remain in close proximity to the bilayer. (**E**) Schematic showing a possible mode of action for epoxy-tiglianes in wound healing.

Fig. 2

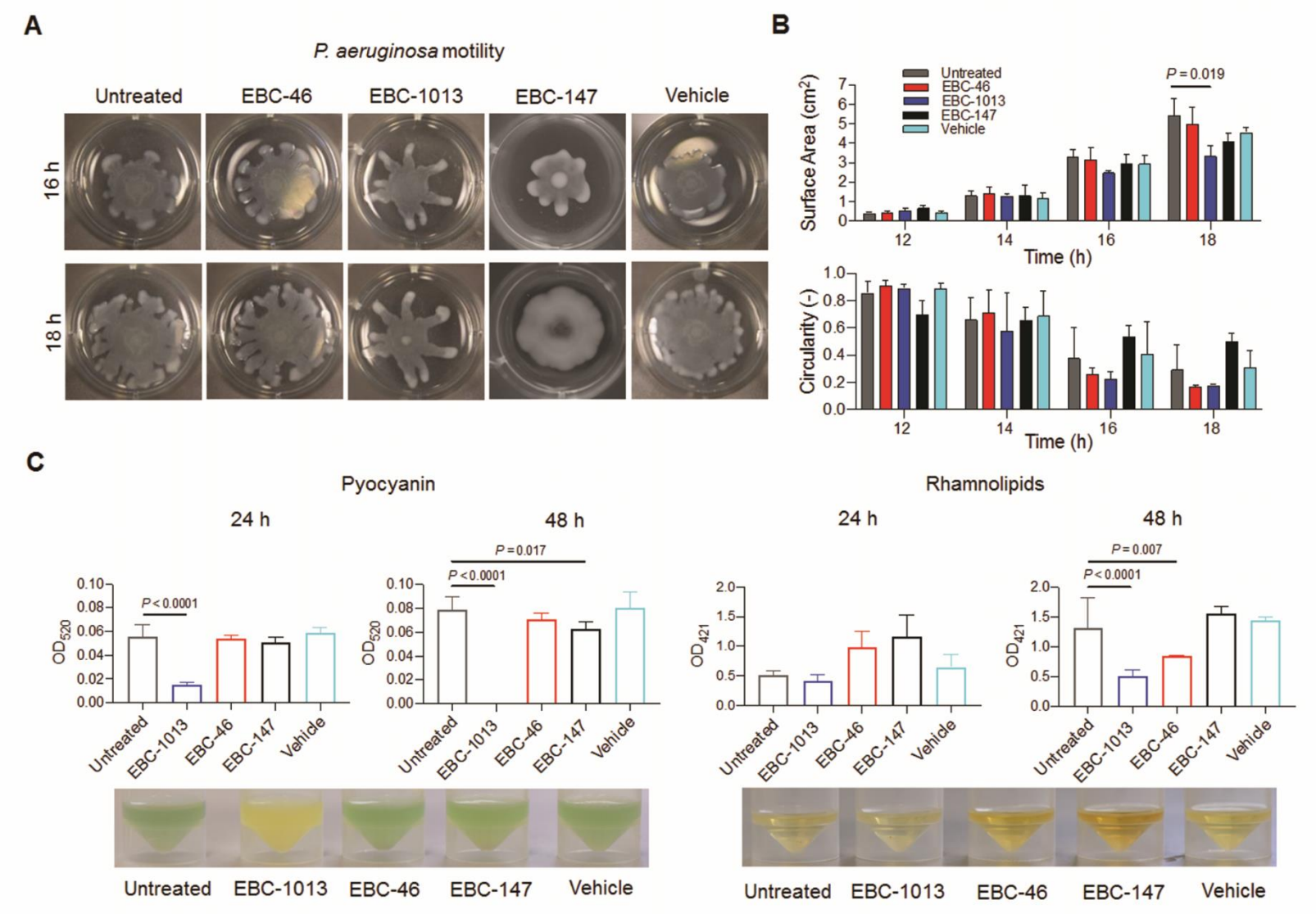
A
P. aeruginosa motility
Untreated
EBC-46
EBC-1013
EBC-147
Vehicle
16 h
18 h
B
Surface Area (cm²)
Untreated
EBC-46
EBC-1013
EBC-147
Vehicle
P = 0.019
Time (h)
Circularity (-)
Time (h)
C
Pyocyanin
24 h
48 h
P < 0.0001
P = 0.017
P < 0.0001
OD520
Rhamnolipids
24 h
48 h
P = 0.007
P < 0.0001
OD421
Untreated
EBC-1013
EBC-46
EBC-147
Vehicle

Fig. 2. Epoxy-tiglianes modify bacterial motility and virulence. (**A** and **B**) Bacterial swarming motility of *P. aeruginosa* PAO1 on BM2 medium ± EBC-46, EBC-1013 or EBC-147 (256 µg/ml) and vehicle equivalent controls. (**A**) Agar plate (16 and 18 hours) images and (**B**) mean circularity (-) and surface area (cm^2) measurements shown as mean ±SD. Statistical comparisons were made using one-way ANOVA and Tukey's multiple comparison tests (n=3). (**C**) Pyocyanin and rhamnolipid production by *P. aeruginosa* PAO1 from 24 and 48 hour cell-free culture supernatants treated with epoxy-tiglianes (256 µg/ml) shown as mean ±SD. Statistical comparisons were made using one way ANOVA with Dunnett's multiple comparisons test (n=3). Photographs of supernatants at 24 hours are shown below. OD_{520} and OD_{421}, optical density at the wavelengths 520 nm and 421 nm respectively.

Fig. 3

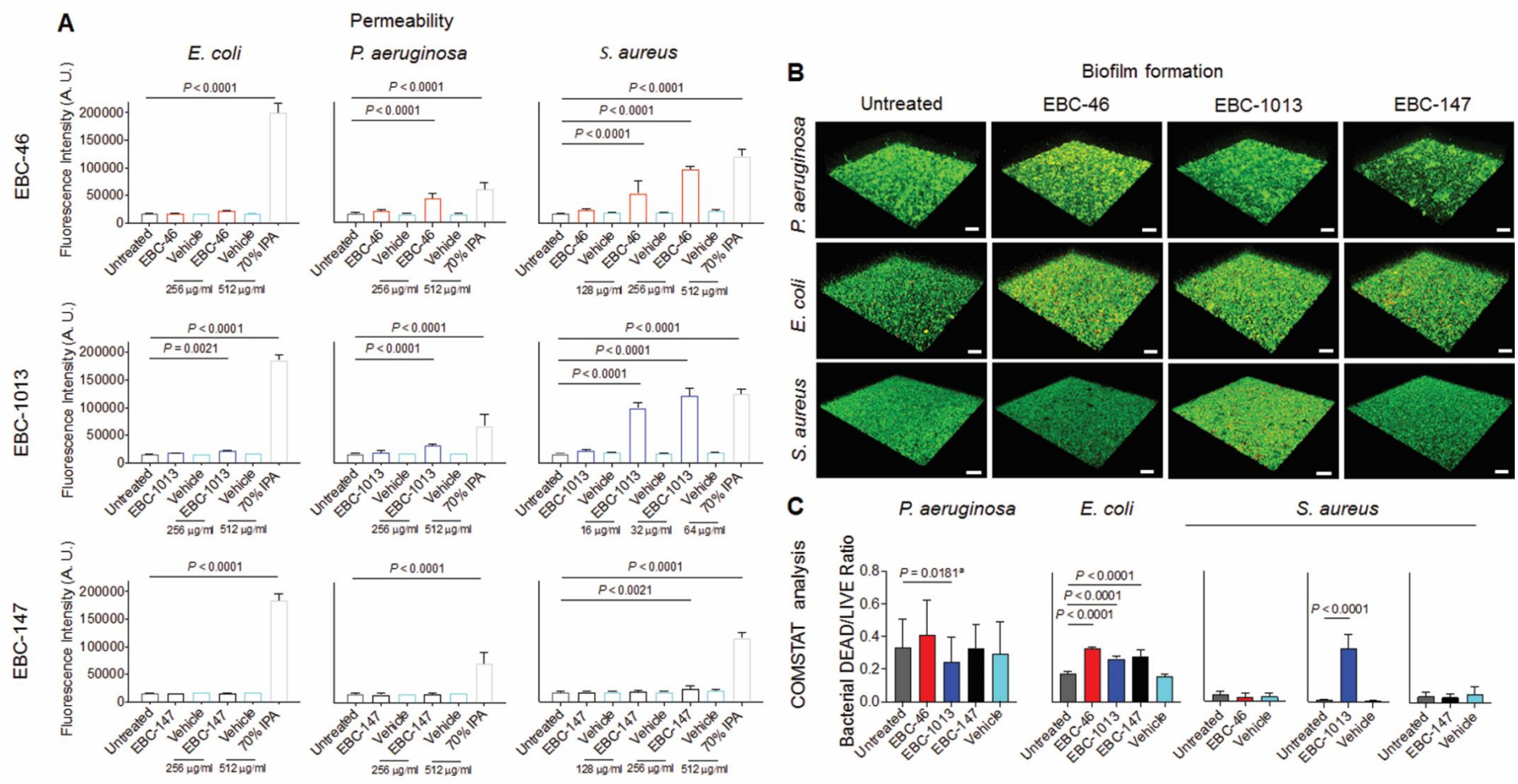
A
Permeability
E. coli
P. aeruginosa
S. aureus
EBC-46
EBC-1013
EBC-147
Fluorescence Intensity (A. U.)
B
Biofilm formation
Untreated
EBC-46
EBC-1013
EBC-147
P. aeruginosa
E. coli
S. aureus
C
COMSTAT analysis
Bacterial DEAD/LIVE Ratio
P. aeruginosa
E. coli
S. aureus
P = 0.0181ª
P < 0.0001
P < 0.0021
P = 0.0021

Fig. 3. Epoxy-tiglianes modify membrane integrity and inhibit biofilm formation. (**A**) Cell membrane permeabilization of *E. coli* IR57, *P. aeruginosa* PAO1 and *S. aureus* 1004A (MRSA) cells by epoxy-tigliane treatment (16 to512 µg/ml) and 70% isopropyl alcohol control (IPA), alongside untreated and vehicle equivalent controls. Results are expressed as mean relative fluorescence intensity ± SD. A.U., arbitrary units. Statistical comparisons were made using one-way ANOVA and Dunnett's multiple comparisons tests (n=3). (**B**) CLSM images of 24 hour biofilm formation following treatment with EBC-46, EBC-1013 and EBC-147 (alongside untreated and vehicle equivalent controls) for Gram-positive *S. aureus* 1004A (tested at MIC: 256, 512 and 512 µg/ml respectively) and Gram-negative *P. aeruginosa* PAO1 and *E. coli* IR57 (both tested at 256 µg/ml as without MIC), n≥3. Scale bar, 30 µm. (**C**) Associated DEAD/LIVE ratio (-) COMSTAT image analysis. Statistical comparisons were made using Kruskal-Wallis test and Mann-Whitney U multiple comparison tests (n ≥ 3). [a]Indicates no significant difference between EBC-treated and vehicle control measurements ($P > 0.05$). All results are expressed as means ± SD.

Fig. 4

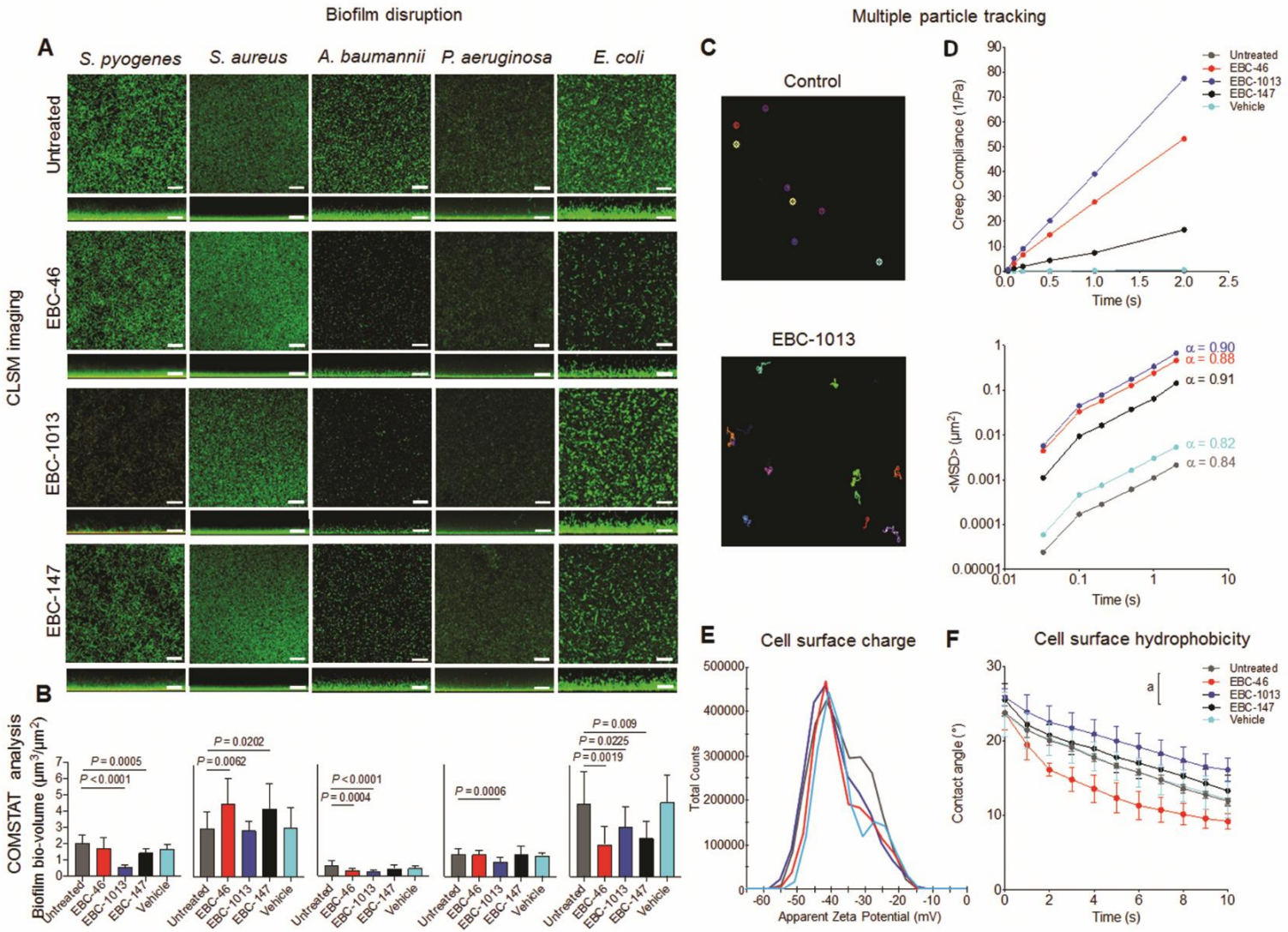
Biofilm disruption
A
S. pyogenes
S. aureus
A. baumannii
P. aeruginosa
E. coli
Untreated
EBC-46
EBC-1013
EBC-147
CLSM imaging
B
COMSTAT analysis
Biofilm bio-volume (μm³/μm²)
P = 0.0005
P < 0.0001
P = 0.0202
P = 0.0062
P < 0.0001
P = 0.0004
P = 0.0006
P = 0.009
P = 0.0225
P = 0.0019
Untreated
EBC-46
EBC-1013
EBC-147
Vehicle
Multiple particle tracking
C
Control
EBC-1013
D
Creep Compliance (1/Pa)
Time (s)
Untreated
EBC-46
EBC-1013
EBC-147
Vehicle
<MSD> (μm²)
α = 0.90
α = 0.88
α = 0.91
α = 0.82
α = 0.84
Time (s)
E
Cell surface charge
Total Counts
Apparent Zeta Potential (mV)
F
Cell surface hydrophobicity
Contact angle (°)
a
Time (s)

Fig. 4. Epoxy-tiglianes induce disruption of established biofilms, modifying biofilm structure, mechanical properties and hydrophobicity. Biofilm disruption assay of wound isolates, *S. pyogenes* E80, *S. aureus* (MRSA) 1004A, *A. baumannii* 7789, *P. aeruginosa* PAO1 and *E. coli* IR57, showing (**A**) CLSM images (scale bars, 30 μm) and (**B**) biofilm biovolume ($\mu m^3/\mu m^2$) COMSTAT image analysis of 24 hour grown biofilms treated with 256 μg/ml epoxy-tigliane compounds (EBC-46, EBC-1013 and EBC-147) for a further 24 hours, alongside untreated and vehicle equivalent controls (means ± SD). Statistical comparisons were made using Kruskal-Wallis test and Mann-Whitney U multiple comparisons tests (n=3). (**C**) Microscopy images showing particle trajectories of 200 nm negatively charged carboxylate FluoSpheres within untreated and 256 μg/ml EBC-1013-treated *E. coli* IR57 biofilms, achieved using multiple particle tracking (MPT). (**D**) Exponential anomalous values (α) of EBC-treated *E. coli* IR57 biofilms, alongside untreated and vehicle equivalent controls, using 200 nm negatively charged carboxylate FluoSpheres. α is based on the relation between the ensemble mean square displacement (MSD) versus time scale of the traced FluoSphere particles and reflects the microrheological degree of resistance of the biofilm towards traced particles where $\alpha > 0.5$ indicates viscous resistance and $\alpha < 0.5$ indicates elastic resistance. <MSD> (μm^2) represents the geometric MSD mean of 360 particles (n=3). Creep compliance (J(T); 1/Pa) of *E. coli* IR57 biofilms representing deformation in response to EBC treatment, alongside untreated and vehicle equivalent controls (n=3). (**E**) Zeta potential (surface charge; mV) distributions for *E. coli* IR57 following 256 μg/ml EBC treatment with untreated and vehicle equivalent controls. (**F**) Contact angle (°) of 256 μg/ml EBC-treated *E. coli* IR57 cells (means ± SD; 20 images/s), alongside untreated and vehicle equivalent controls ($n \geq 3$). Minimum significant difference (^{a}) was calculated using ANOVA analysis followed by Tukey-Kramer post hoc test ($P < 0.05$).

Fig. 5

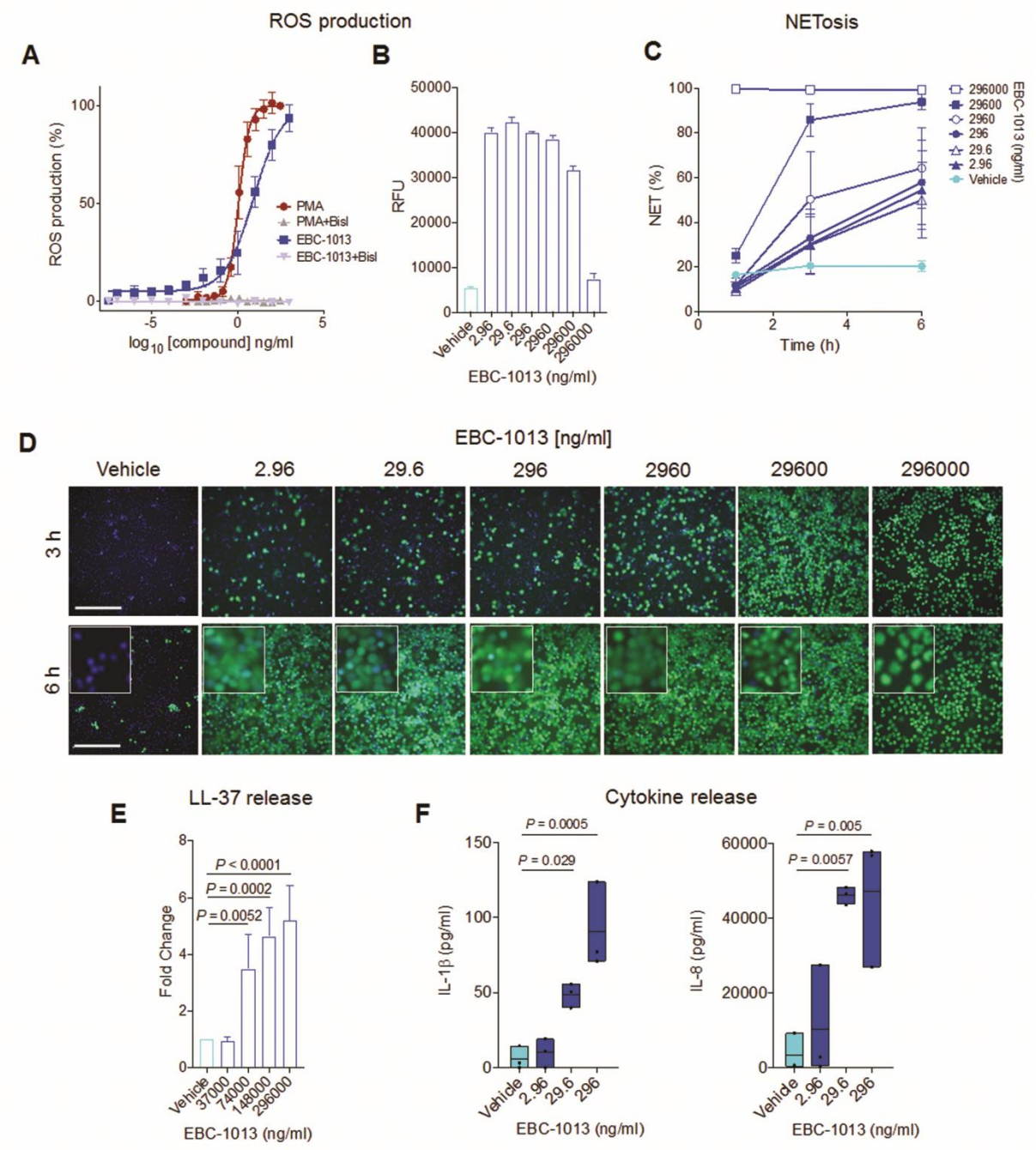
ROS production
A
ROS production (%)
log10 [compound] ng/ml
PMA
PMA+Bisl
EBC-1013
EBC-1013+Bisl
B
RFU
Vehicle
2.96
29.6
296
2960
29600
296000
EBC-1013 (ng/ml)
NETosis
C
NET (%)
Time (h)
296000
29600
2960
296
29.6
2.96
Vehicle
EBC-1013 (ng/ml)
D
EBC-1013 [ng/ml]
Vehicle
2.96
29.6
296
2960
29600
296000
3 h
6 h
E
LL-37 release
Fold Change
P < 0.0001
P = 0.0002
P = 0.0052
Vehicle
37000
74000
148000
296000
EBC-1013 (ng/ml)
F
Cytokine release
IL-1β (pg/ml)
P = 0.0005
P = 0.029
Vehicle
2.96
29.6
296
EBC-1013 (ng/ml)
IL-8 (pg/ml)
P = 0.005
P = 0.0057
Vehicle
2.96
29.6
296
EBC-1013 (ng/ml)

Fig. 5. EBC-1013 induces antibacterial/inflammatory activity in PMNLs and PBMCs in vitro. (**A**) EBC-1013/PMA ± 4 μM PKC-inhibitor bisindolylmaleimide I (BisI) dose-response experiments performed with PMNLs to determine mean EC_{50} values [% reactive oxygen species (ROS); compared to PMA-induced maximal ROS production]; EBC-1013/PMA (n=4); EBC-1013/PMA + BisI (n=1). Data shown as meanS ±SD. (**B**) EBC-1013 (or vehicle) dose-response experiments to investigate ROS production in PMNLs over a broader concentration range (n=2). RFU (relative fluorescence units) was determined 1 hour after treatment. Data shown as mean ±SD. (**C**) Percentage of cells undergoing NETosis (i.e. proportion of $Hoescht^+$ and SYTOX $Green^+$ stained cells) following EBC-1013 (or vehicle) treatment (1 to 6 hours), measured with QuPath image analysis software (n=3). Data shown as means ± SEM. (**D**) Representative images of EBC-1013-induced NETosis in PMNLs [stained with Hoescht 33342 (blue) and SYTOX Green (green)], acquired at 3 and 6 hours with a 10x objective lens. Inset-magnified areas show NETosis at lower concentrations (diffuse staining: 2.96 to 29,600 ng/ml) and necrosis at higher doses (compact staining: 296,000 ng/ml). Scale bars, 200 μm. (**E**) LL-37 release from PMNLs (3 hour treatment with EBC-1013) compared to the vehicle, measured by ELISA of cell culture supernatants, (n=4). Data shown as means ±SD. Statistical comparisons were made using a one-way ANOVA and Dunnett's multiple comparisons tests. (**F**) Floating bar graphs of EBC-1013 (or vehicle) stimulation of IL-1β and IL-8 secretion from PBMCs (24 hour treatment) analyzed via flow cytometry using a BD cytometric bead array of cell culture supernatants (n=3). The box in the graph encompasses the maximum and minimum values, the line represents the mean and the dots represent the individual data points. Statistical comparisons were made using one-way ANOVA and Dunnett's multiple comparisons tests.

Fig. 6

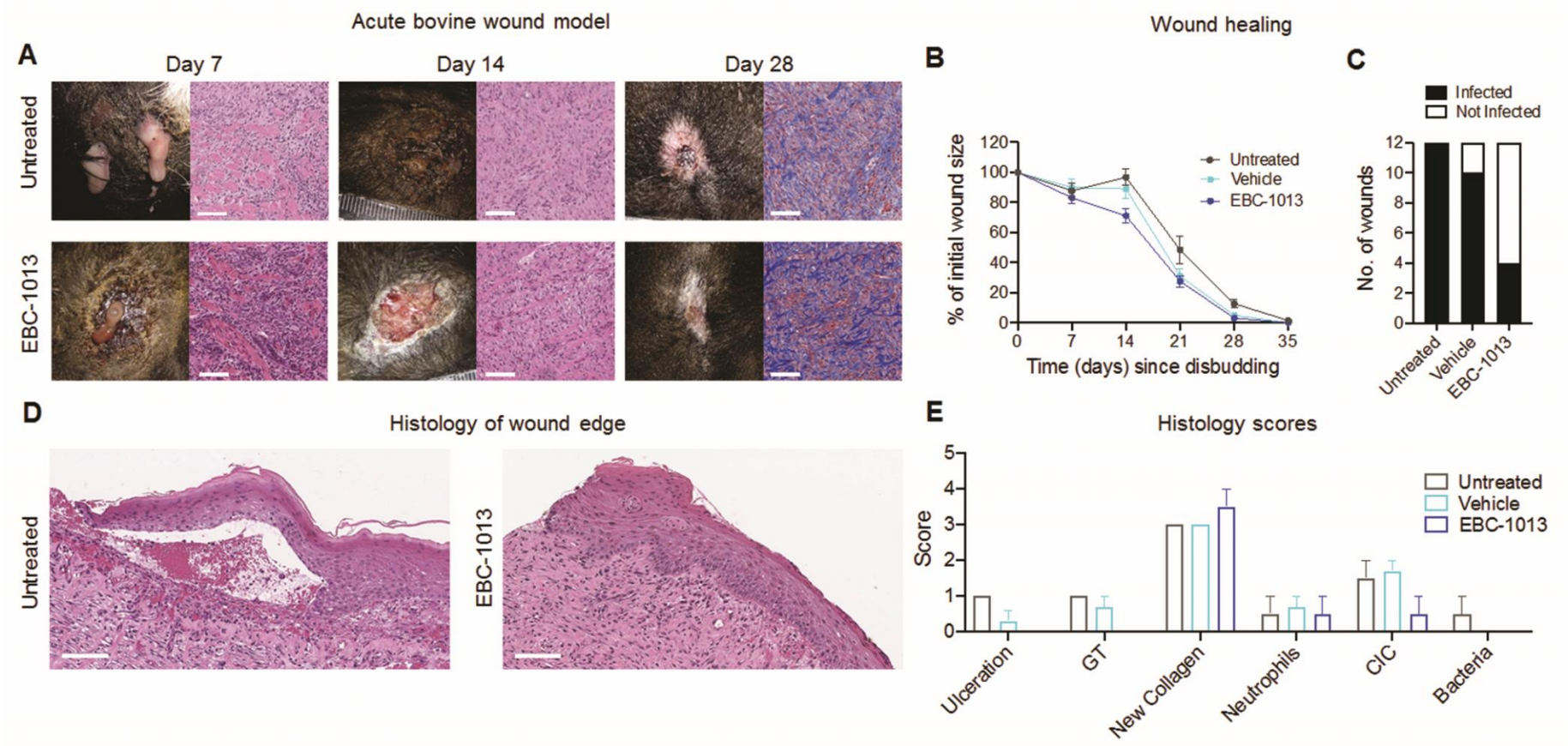
Acute bovine wound model
A
Day 7
Day 14
Day 28
Untreated
EBC-1013
Wound healing
B
% of initial wound size
Time (days) since disbudding
Untreated
Vehicle
EBC-1013
C
Infected
Not Infected
No. of wounds
Untreated
Vehicle
EBC-1013
D
Histology of wound edge
Untreated
EBC-1013
E
Histology scores
Score
Untreated
Vehicle
EBC-1013
Ulceration
GT
New Collagen
Neutrophils
CIC
Bacteria

Fig. 6. EBC-1013 promotes resolution of infection and wound closure (healing) in acute calf thermal burn injury wounds. (**A**) Time series images (days 7, 14 and 28) of healing calf wounds ± EBC-1013 treatment (3 mg/ml; n = 12) with corresponding micrographs of wound biopsies at each time point stained with either hematoxylin and eosin (H&E) (days 7 and 14) or Masson's stain (day 28). Scale bars, 100 μm. Day 7, infection and suppurating wounds observed; day 14, wound infection continuing in all control wounds, while EBC-1013-treated wounds appeared granulated and healing well; day 28, resolution of infection and wound closure in the EBC-1013-treated wounds. (**B**) Percentage reduction in wound area over 35 days for control, vehicle and EBC-1013-treated wounds (mean ± SEM). (**C**) Clinical infection (Number of infected/not infected wounds) observed at day 14 in control, vehicle- and EBC-1013-treated wounds. (**D**) Histology from wound edge biopsies at day 28 demonstrating superior healing with EBC-1013 treatment. Scale bars, 100 μm. **(E**) Semiquantitative histological analysis (scores 1 to 4) of wound biopsies from control, vehicle and EBC-1013 treated wounds taken at day 28 after injury. GT, granulation tissue; CIC, chronic inflammatory cells. Data shown as means ±SEM.

Fig. 7

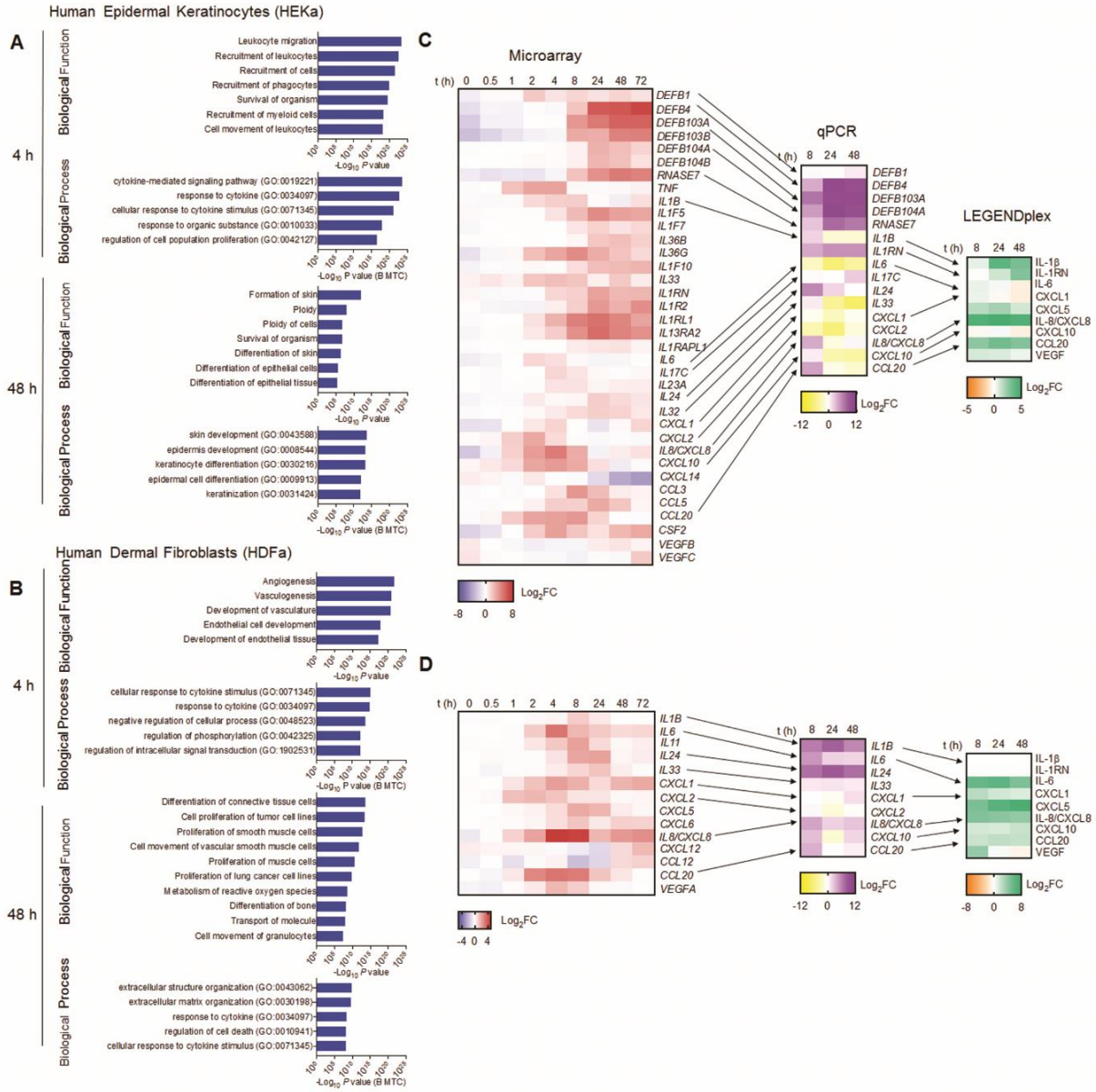
Human Epidermal Keratinocytes (HEKa)
A
4 h
Biological Function
Leukocyte migration
Recruitment of leukocytes
Recruitment of cells
Recruitment of phagocytes
Survival of organism
Recruitment of myeloid cells
Cell movement of leukocytes
Biological Process
cytokine-mediated signaling pathway (GO:0019221)
response to cytokine (GO:0034097)
cellular response to cytokine stimulus (GO:0071345)
response to organic substance (GO:0010033)
regulation of cell population proliferation (GO:0042127)
-Log10 P value
48 h
Biological Function
Formation of skin
Ploidy
Ploidy of cells
Survival of organism
Differentiation of skin
Differentiation of epithelial cells
Differentiation of epithelial tissue
Biological Process
skin development (GO:0043588)
epidermis development (GO:0008544)
keratinocyte differentiation (GO:0030216)
epidermal cell differentiation (GO:0009913)
keratinization (GO:0031424)
-Log10 P value (B MTC)
Human Dermal Fibroblasts (HDFa)
B
4 h
Biological Function
Angiogenesis
Vasculogenesis
Development of vasculature
Endothelial cell development
Development of endothelial tissue
Biological Process
cellular response to cytokine stimulus (GO:0071345)
response to cytokine (GO:0034097)
negative regulation of cellular process (GO:0048523)
regulation of phosphorylation (GO:0042325)
regulation of intracellular signal transduction (GO:1902531)
-Log10 P value (B MTC)
48 h
Biological Function
Differentiation of connective tissue cells
Cell proliferation of tumor cell lines
Proliferation of smooth muscle cells
Cell movement of vascular smooth muscle cells
Proliferation of muscle cells
Proliferation of lung cancer cell lines
Metabolism of reactive oxygen species
Differentiation of bone
Transport of molecule
Cell movement of granulocytes
Biological Process
extracellular structure organization (GO:0043062)
extracellular matrix organization (GO:0030198)
response to cytokine (GO:0034097)
regulation of cell death (GO:0010941)
cellular response to cytokine stimulus (GO:0071345)
-Log10 P value
-Log10 P value (B MTC)
C
Microarray
t (h) 0 0.5 1 2 4 8 24 48 72
DEFB1
DEFB4
DEFB103A
DEFB103B
DEFB104A
DEFB104B
RNASE7
TNF
IL1B
IL1F5
IL1F7
IL36B
IL36G
IL1F10
IL33
IL1RN
IL1R2
IL1RL1
IL13RA2
IL1RAPL1
IL6
IL17C
IL23A
IL24
IL32
CXCL1
CXCL2
IL8/CXCL8
CXCL10
CXCL14
CCL3
CCL5
CCL20
CSF2
VEGFB
VEGFC
Log2FC
-8 0 8
qPCR
t (h) 8 24 48
DEFB1
DEFB4
DEFB103A
DEFB104A
RNASE7
IL1B
IL1RN
IL6
IL17C
IL24
IL33
CXCL1
CXCL2
IL8/CXCL8
CXCL10
CCL20
Log2FC
-12 0 12
LEGENDplex
t (h) 8 24 48
IL-1β
IL-1RN
IL-6
CXCL1
CXCL5
IL-8/CXCL8
CXCL10
CCL20
VEGF
Log2FC
-5 0 5
D
t (h) 0 0.5 1 2 4 8 24 48 72
IL1B
IL6
IL11
IL24
IL33
CXCL1
CXCL2
CXCL5
CXCL6
IL8/CXCL8
CXCL12
CCL12
CCL20
VEGFA
Log2FC
-4 0 4
t (h) 8 24 48
IL1B
IL6
IL24
IL33
CXCL1
CXCL2
IL8/CXCL8
CXCL10
CCL20
Log2FC
-12 0 12
t (h) 8 24 48
IL-1β
IL-1RN
IL-6
CXCL1
CXCL5
IL-8/CXCL8
CXCL10
CCL20
VEGF
Log2FC
-8 0 8

Fig. 7. EBC-1013 treatment promotes expression of host-defense peptides, inflammatory cytokine/chemokines and proresolution genes in human keratinocytes/fibroblasts in vitro. Analysis of expression profiling using the HumanHT-12 v4 microarray ± EBC-1013. (**A** and **B**) Top-ranking biological function terms from Ingenuity Pathway Analysis (IPA) and biological process terms from Gene Ontology Analysis (GO) following expression profiling of 100 ng/ml EBC-1013-treated (**A**) HEKa and (**B**) HDFa cells at 4 and 48 hours. BMTC, Bonferroni multiple testing correction. (**C** and **D**) Heatmap representation of selected targets from microarray profiling data, qPCR or LEGENDplex quantification. LEGENDplex data shows the indicated cytokines/chemokines/growth factors released in response to 100 ng/ml EBC-1013 treatment [compared to vehicle (ethanol)] in (**C**) HEKa and (**D**) HDFa cells. Results are expressed as log_2FC values (n=3 for qPCR and LEGENDplex analyses).

Fig. 8

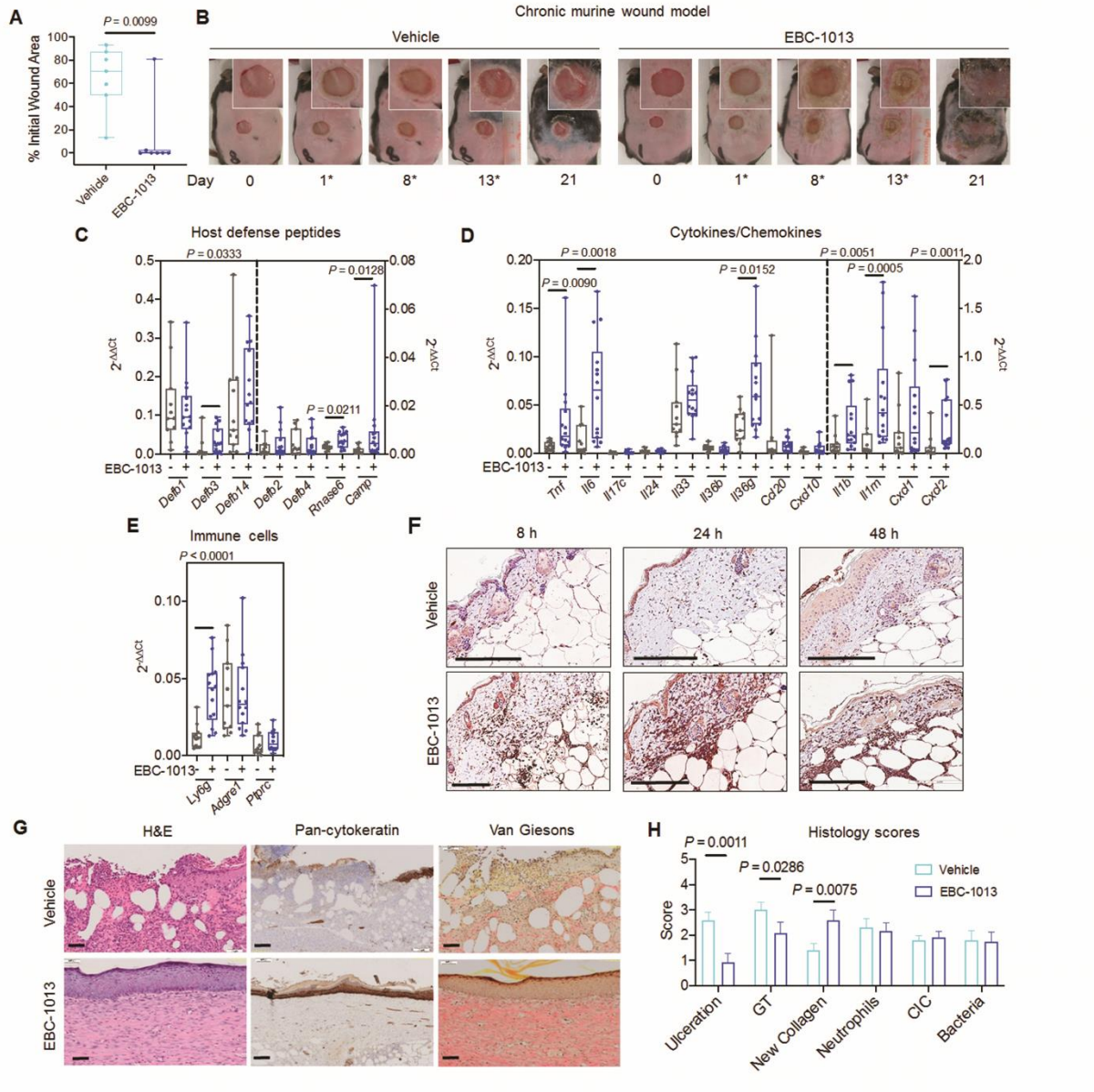
A
P = 0.0099
% Initial Wound Area
Vehicle
EBC-1013
B
Chronic murine wound model
Vehicle
EBC-1013
Day 0 1* 8* 13* 21
C
Host defense peptides
P = 0.0333
P = 0.0128
P = 0.0211
2^-ΔΔCt
EBC-1013
Defb1 Defb3 Defb14 Defb2 Defb4 Rnase6 Camp
D
Cytokines/Chemokines
P = 0.0018
P = 0.0090
P = 0.0152
P = 0.0051
P = 0.0005
P = 0.0011
Tnf Il6 Il17c Il24 Il33 Il36b Il36g Cxcl20 Cxcl10 Il1b Il1rn Cxcl1 Cxcl2
E
Immune cells
P < 0.0001
Ly6g Adgre1 Ptprc
F
8 h
24 h
48 h
Vehicle
EBC-1013
G
H&E
Pan-cytokeratin
Van Giesons
Vehicle
EBC-1013
H
Histology scores
P = 0.0011
P = 0.0286
P = 0.0075
Vehicle
EBC-1013
Score
Ulceration GT New Collagen Neutrophils CIC Bacteria

Fig. 8. EBC-1013-directed healing in a murine model of chronic wounds is associated with the upregulated expression of host-defense peptides, cytokines/chemokines and PMNL infiltration. (**A** and **B**) Healing in skin wounds from aged diabetic *db/db* mice (> 6 months old) housed in non-sterile conditions treated with vehicle/EBC-1013 (0.3 mg/ml). (**A**) Wound closure measurements at cull (days 21 to 29), expressed as percentage of the initial wound area, in mice treated with vehicle/EBC-1013 (n=7). The data is represented as a box-and-whisker plot where the boxes encompass the 25th to 75th percentiles, the line is at the median, the whiskers represent the range and the dots are the individual data points. *P* values were calculated by Mann-Whitney U test. (**B**) Images from a single wound taken at 0, 1, 8, 13 and 21 days (with inset-magnified images) are shown. (Healing in all seven wounds is shown in fig. S10). Mice were treated on days 1, 8 and 13, as indicated (*). qPCR analysis of EBC-1013-treated wounds revealing changes in selected (**C**) host defense peptide, (**D**) cytokine/chemokine and (**E**) immune cell marker genes. RNA acquired from vehicle- and EBC-1013-treated wounds (24 hours) was analyzed using primers for the indicated gene sets. Data are expressed as $2^{-\Delta\Delta Ct}$ values. *B2m* mRNA and *Gapdh* mRNA (fig. S11) were used as the normalization controls. Vehicle, (n=11); EBC-1013, (n=14). The data is represented as a box-and-whisker plot (see above). *P* values were calculated by Mann-Whitney U test. (**F**) Analysis of PMNL infiltration into EBC-1013-treated wounds. Immunohistochemistry performed on formalin-fixed paraffin-embedded (FFPE) sections using an anti-Ly6G antibody. Representative images shown for vehicle/EBC-1013 treated wounds at 8, 24 and 48 hours (n=6). Scale bars, 200 μm. (**G**) Representative light micrographs of vehicle- and EBC-1013-treated wound biopsies at day 21 stained with either Van Giesons, Pancytokeratin or H&E (n=8). Scale bars, 50 μm. (**H**) Semiquantitative histological analysis (scores 1 to 4) of wound biopsies from vehicle/EBC-1013 treated wounds taken at cull. GT, granulation tissue; CIC, chronic inflammatory cells. *P* values were calculated by Mann-Whitney U test.

392